Cellular/Molecular

Ca²⁺ Channel to Synaptic Vesicle Distance Accounts for the Readily Releasable Pool Kinetics at a Functionally Mature Auditory Synapse

Zuxin Chen,[1] **Brati Das,**[1,2] **Yukihiro Nakamura,**[3,4] **David A. DiGregorio,**[3,4] **and Samuel M. Young, Jr**[1]

[1]Research Group Molecular Mechanisms of Synaptic Function, Max Planck Florida Institute, Jupiter, Florida 33458, [2]Integrative Program in Biology and Neuroscience, Florida Atlantic University, Jupiter, Florida 33458, [3]Laboratory of Dynamic Neuronal Imaging, Institut Pasteur, 75724 Paris Cedex 15, France, and [4]CNRS UMR 3571, 75724 Paris Cedex 15, France

Precise regulation of synaptic vesicle (SV) release at the calyx of Held is critical for auditory processing. At the prehearing calyx of Held, synchronous and asynchronous release is mediated by fast and slow releasing SVs within the readily releasable pool (RRP). However, the posthearing calyx has dramatically different release properties. Whether developmental alterations in RRP properties contribute to the accelerated release time course found in posthearing calyces is not known. To study these questions, we performed paired patch-clamp recordings, deconvolution analysis, and numerical simulations of buffered Ca²⁺ diffusion and SV release in postnatal day (P) 16–19 mouse calyces, as their release properties resemble mature calyces of Held. We found the P16–P19 calyx RRP consists of two pools: a fast pool ($\tau \leq 0.9$ ms) and slow pool ($\tau \sim 4$ ms), in which release kinetics and relative composition of the two pools were unaffected by 5 mM EGTA. Simulations of SV release from the RRP revealed that two populations of SVs were necessary to reproduce the experimental release rates: (1) SVs located close (∼5–25 nm) and (2) more distal (25–100 nm) to VGCC clusters. This positional coupling was confirmed by experiments showing 20 mM EGTA preferentially blocked distally coupled SVs. Lowering external [Ca²⁺] to *in vivo* levels reduced only the fraction SVs released from the fast pool. Therefore, we conclude that a dominant parameter regulating the mature calyx RRP release kinetics is the distance between SVs and VGCC clusters.

Key words: active zone; calcium channels; calyx of Held; priming; readily releasable pool; synaptic vesicle

Introduction

The availability of fusion competent synaptic vesicles (SVs), the readily releasable pool (RRP) for action potential (AP) release, is a major determinant of the range of the bandwidth that a synapse can transmit information (Neher, 2010). Sound encoding within the first few auditory processing stations in the lower auditory brainstem requires the synaptic connections to transmit information in response to a wide range of AP firing rates, up to the kilohertz range (Grothe et al., 2010). Because of its large size, experimental accessibility, and similar release probability to other synapses (Borst, 2010), the calyx of Held/medial nucleus of

the trapezoid body (MNTB) synapse is a model quantifying RRP properties for such high bandwidth transmission (Borst, 2010; Borst and Soria van Hoeve, 2012). Previous studies have shown that, before hearing onset, postnatal day (P) 8–11, the calyx RRP of SVs depletes over 2 distinct release time constants, indicating the presence of "fast" and "slow" SV subpools (Sakaba and Neher, 2001b). The "fast" pool underpins synchronous release of SVs in response to APs, whereas the "slow" pool consists of asynchronously released SVs during high-frequency AP trains and long depolarizations (Sakaba, 2006).

After hearing onset, the calyx of Held undergoes developmental transformations that increase the speed and fidelity of synchronous AP-evoked release to sustain and drive AP spiking in the MNTB upwards to 1 kHz (Taschenberger and von Gersdorff, 2000), with little to no asynchronous release (Scheuss et al., 2007). The lack of asynchronous release raises questions whether a slow pool exists, let alone its role in auditory processing. Even in prehearing calyces, the cellular mechanisms underlying the slow pool is under debate; either (1) SVs are positioned at different distances with respect to voltage-gated Ca²⁺ channels (VGCCs) (Wadel et al., 2007) or (2) SVs exhibit intrinsic differences in Ca²⁺ sensitivity (Wolfel et al., 2007). Moreover, a study of RRP dynamics in the mature calyx is lacking, resulting in uncertainties in how precise transmission necessary for auditory processing is achieved.

To uncover mechanisms determining SV availability within the RRP for fast synchronous release, we examined RRP properties of the P16–P19 calyx of Held, which has similar release properties to the mature calyx (Fedchyshyn and Wang, 2005; Lorteije et al., 2009; Sonntag et al., 2009; Sonntag et al., 2011). Paired whole-cell patch-clamp recordings followed by deconvolution analysis revealed that the RRP at P16–P19 depleted faster than in prehearing calyces (P9–P11) but still exhibited two decay time constants ($\tau \leq 0.9$ ms, $\tau \sim 4$ ms) with a ratio of ~2:1 (fast/slow). The release kinetics and relative composition of the two pools were unaffected by 5 mM EGTA, consistent with the idea that both pools are in close proximity to VGCCs (<100 nm). However, 1.2 mM external Ca^{2+}, which mimics *in vivo* calyx release probabilities (Lorteije et al., 2009), reduced release only from the fast pool. Numerical simulations of buffered Ca^{2+} diffusion and SV release revealed that SVs located close to a cluster of VGCCs accounted for the fast release component, whereas the distal SVs, with the same Ca^{2+} sensitivity, accounted for the slow release kinetics, a prediction confirmed by the preferential inhibition of release of distal vesicles by 20 mM EGTA. We conclude that, at the functionally mature calyx of Held, the distance between SVs and VGCCs is a dominant parameter controlling RRP release kinetics.

Materials and Methods

Animal handling. C57BL/6 mice in two age groups of P9–P11 (immature calyces) and P16–P21 (functionally mature calyces) from either sex were used for all the experiments. All experiments were performed in accordance with the animal welfare laws of the Max Planck Florida Institute for Neuroscience Institutional Animal Care and Use Committee.

Slice preparation. Acute brainstem slices containing the MNTB were prepared from mice using a Leica VT 1200 vibratome (P9–P11: 200-μm-thick slices; P16–P21, 180–220-μm-thick slices). Slices were immediately transferred to an incubation beaker containing standard extracellular solution (at 37°C, continuously bubbled with 95% O_2–5% CO_2) containing the following (in mM): 125.0 NaCl, 2.5 KCl, 1.0 $MgCl_2$, 2.0 $CaCl_2$, 10.0 glucose, 25.0 $NaHCO_3$, 1.25 NaH_2PO_4, 0.4 L-ascorbic acid, 3.0 myo-inositol, and 2.0 Na-pyruvate, pH 7.3–7.4 (310 mOsm). After 45 min of incubation, slices were transferred to a recording chamber with the same saline solution at room temperature (25°C).

Electrophysiology. Recordings were made with a HEKA EPC 10/2 amplifier controlled by Patch-master software (HEKA). Sampling intervals and filter settings were 20–50 μs and 6 kHz, respectively. For paired recordings, presynaptic calyx terminals and principal neurons of MNTB were simultaneously whole-cell voltage-clamped at −80 mV and −60 mV, respectively. Patch pipettes had an open tip resistances of 4.5–5.5 MΩ and 3.5–4.5 MΩ for presynaptic and postsynaptic recordings, respectively. Presynaptic patch pipettes were filled with solutions containing the following (in mM): 130.0 Cs-gluconate, 20.0 TEA-Cl, 10.0 HEPES, 5.0 Na_2-phosphocreatine, 4.0 MgATP, 0.3 NaGTP, and 0.5 EGTA, pH 7.25 (325–340 mOsm). The amount of 0.5 mM is an internal EGTA concentration ($[EGTA]_i$) that separates the fast and slow release components in the prehearing calyx (Sakaba and Neher, 2001b), which we considered "control." To determine how increasing $[EGTA]_i$ affects RRP release kinetics, presynaptic patch pipettes were filled with either 5 or 20 mM EGTA. Osmolality of these solutions was similar to that with 0.5 mM EGTA. In experiments studying the EGTA effect on presynaptic Ca^{2+} currents (I_{Ca}), $[EGTA]_i$ was increased from 0.5 to 5 mM. The series resistance (Rs) for presynaptic recording pipettes was between 8 and 25 MΩ (usually 10–15 MΩ) and compensated to 6–8 MΩ by the HEKA amplifier online. Leak currents in presynaptic recordings were subtracted by a P/4 pulse protocol (Armstrong and Bezanilla, 1974). Postsynaptic patch pipettes were filled with same internal solution as the presynaptic one, except that the $[EGTA]_i$ was increased to 5 mM. Postsynaptic series resistance was between 3 and 8 MΩ and compensated to 3 MΩ online, the remaining Rs was further compensated completely offline with Igor routine. During recordings, the bath solution was supplemented with 1.0 μM TTX (Alomone Labs), 20.0 mM TEA-Cl (Sigma), and 100.0 μM 4-AP

(Sigma) to block voltage-dependent sodium and potassium currents, 50.0 μM D-AP5 to block NMDA receptors, 100.0 μM cyclothiazide (CTZ) and 2.0 mM γ-D-glutamylglycine (γ-DGG) to minimize AMPA receptor desensitization and saturation. D-AP5, CTZ, and γ-DGG were from Tocris Bioscience.

Because the rate of release of the RRP is highly sensitive to step potentials (Sakaba and Neher, 2001a), to measure the RRP release rates, a 2 ms square prepulse from −80 to 70 mV to maximally open VGCCs was applied and then subsequently stepped back to 0 mV, where the steady-state I_{Ca} values are maximal for variable durations. To determine the effect of AP depolarization on I_{Ca}, we used a pseudo AP voltage command waveform from −70 mV to 60 mV, where the depolarization was for 0.2 ms and the repolarization was for 0.4 ms. The raw currents and the total charge integral were compared at the two different $[EGTA]_i$ (Yang and Wang, 2006). To analyze the activation kinetics of VGCCs, we used the tail currents observed after 10 ms depolarizing pulses from −70 mV to 60 mV.

Data analysis. Electrophysiological data were analyzed offline with custom programming written in Igor Pro (version 6.12A; Wavemetrics). Statistics analyses were performed with Prism 5 (GraphPad Software). All averaged data from experiments are shown as mean ± SEM. To compare two different groups, an unpaired Student's *t* test was used. To compare different datasets within the same group, paired Student's *t* test was used. For Figure 8, the tail current amplitude was plotted against voltage and fitted with the Boltzmann function $I = 1/(I_{max} + \exp(V_{\frac{1}{2}} - V)/k)$, where $V_{\frac{1}{2}}$ and k represent the half-activation voltage and slope factor, respectively. For EPSC analysis, EPSC amplitudes were measured as peak minus baseline. Synaptic delays in response to step depolarization (step) were defined as the duration between the onset of the I_{Ca} and the time at which the EPSCs were 50% of their maximum. To estimate the presynaptic I_{Ca} charge, the presynaptic I_{Ca} was integrated. For the 1 ms step, the Ca^{2+} charges were measured from the onset of the Ca^{2+} influx to the point where 10% of the peak I_{Ca} remained. For other longer steps, the Ca^{2+} charge was measured from the onset of the Ca^{2+} influx to the time of the peak of the tail currents, which were generated by stepping the presynaptic voltage back to holding potential.

Deconvolution analysis. We used a deconvolution method to estimate quantal release rates using a previously established method for the calyx of Held synapse (Neher and Sakaba, 2001b; Sakaba and Neher, 2001b, c, a). This method takes into account clearance of residual glutamate in the synaptic cleft (Neher and Sakaba, 2001a, b; Sakaba and Neher, 2001b). The quantal size for EPSC deconvolution is based on methods introduced by Neher and Sakaba (2001a, b). To determine quantal release rates, a template miniature EPSC (mEPSC) waveform was empirically generated for each paired recording using a macro based on Neher and Sakaba (2001a, b). The mEPSC waveform generated for each paired recording used an average mEPSC amplitude specific for the P9–P11 or P16–P19 mouse calyx (Wang et al., 2008), while the mEPSC fast and slow time constant of decay was determined by varying the time constants of decay and their relative amplitude (macro based on Neher and Sakaba, 2001a, b). Briefly, the residual current was estimated using presynaptic depolarizations of different durations to estimate the residual current due to slow glutamate clearance (macro based on Neher and Sakaba, 2001a, b). Under the recording conditions used, the residual current is the major slow decay component in the EPSC recorded from the prehearing calyx synapses (Neher and Sakaba, 2001b; Sakaba and Neher, 2001a, b, c). However by P16, there is a small residual current in the calyx/MNTB cleft (Joshi et al., 2004; Renden et al., 2005), consistent with little to no contribution of slow glutamate clearance to the EPSC waveform at P16–P19 under the recording conditions used (Wang et al., 2008). Although the deconvolution analysis yields an accurate estimate of the fast release component, caution must be taken for measuring the slow vesicle release as they can be influenced by parameters used for the residual glutamate current. However, the negligible slow components in the P16–P19 calyx are not subject to potential issues with fitting of the spillover current. Quantal release rates were subsequently integrated to obtain the cumulative release to estimate the RRP size. For the long depolarization step for 30 ms in the P9–P11 group and for 10 ms in the P16–P19 group, the cumulative release was further corrected for the refilling of SVs during the stimulation; the average refilling rate was 10 SVs/ms in both P9–P11 and P16–P19 groups under our experimental condition. For the experiments
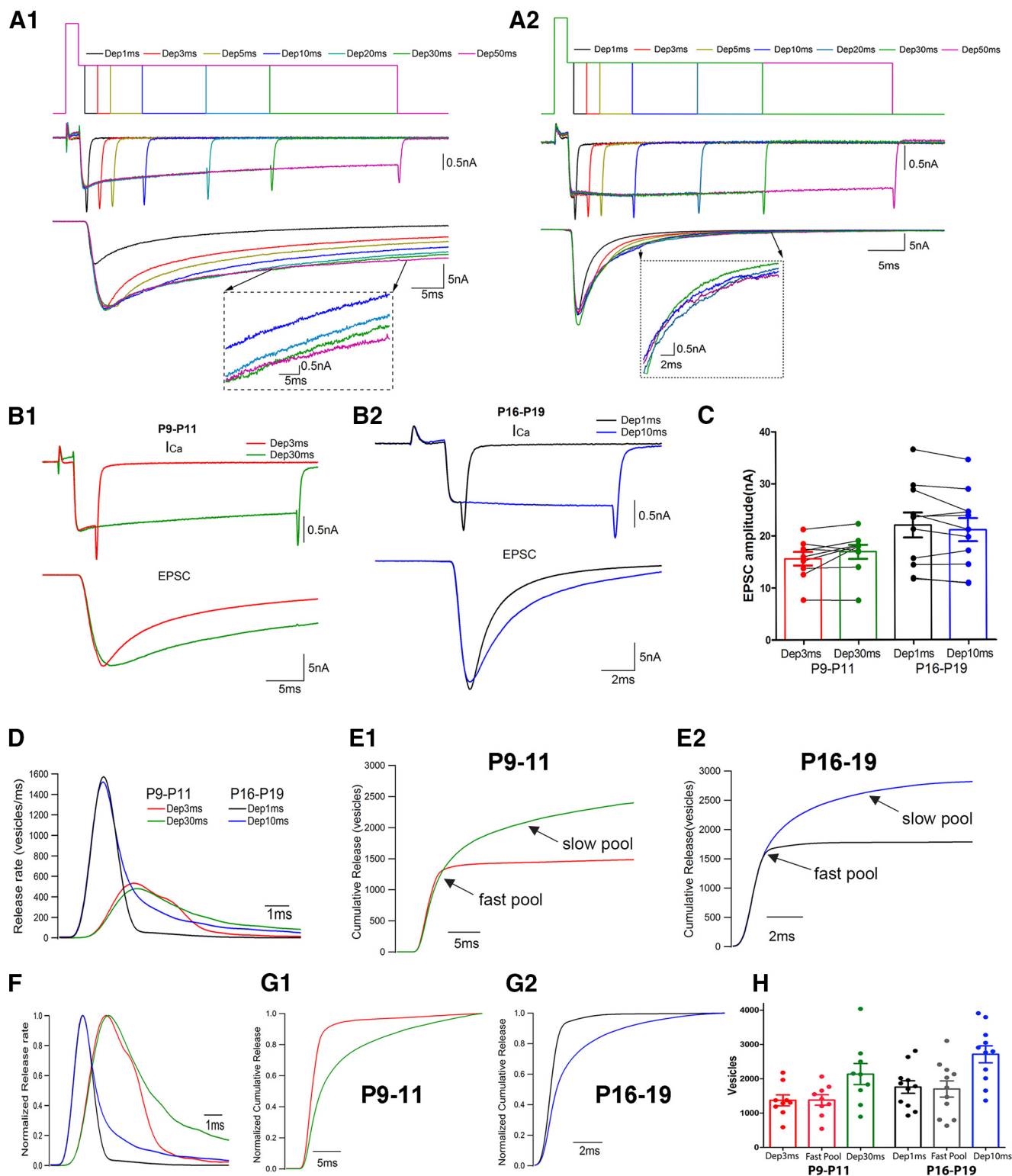
Figure 1. The speed of synaptic transmission is increased with development at the calyx of Held/MNTB synapse. **A1**, **A2**, Presynaptic stimulation protocol. Top, The presynaptic potential was depolarized to 70 mV for 2 ms, followed by 0 mV for 1, 3, 5, 10, 20, 30, and 50 ms. The duration of 0 mV and the related responses are labeled as Dep1 ms, Dep3 ms, Dep5 ms, Dep10 ms, Dep20 ms, Dep30 ms, and Dep50 ms, respectively. Middle, Resulting presynaptic I_{Ca} values. Bottom, Corresponding EPSCs. Dashed line box represents a magnified view of the decaying EPSCs. **A1**, Representative traces from P9–P11 mice. **A2**, Representative traces from P16–P19 mice. **B1**, **B2**, Average traces of I_{Ca} (top) and corresponding average traces of EPSCs (middle). **B1**, P9–P11 mice. Red traces represent Dep3 ms. Green traces represent Dep30 ms. **B2**, P16–P19 mice. Black traces represent Dep1 ms. Blue traces represent Dep10 ms. **C**, Summary data for EPSC amplitudes. EPSCs are from Dep3 ms and Dep30 ms in P9–P11 mice (9 pairs) and from Dep1 ms and Dep10 ms in P16–P19 mice (11 pairs). Data are presented as mean ± SEM. **D**, Average release rate trace. **E1**, **E2**, Cumulative release from P9–P11 synapses (**E1**) and P16–P19 synapses (**E2**). Arrow points to the fast rising and slowly rising phase of the curve, which is contributed by fast pool and slow pool, respectively. **F**, Normalized average release rate. **G1**, Normalized cumulative release from P9–P11 synapses. The endpoint of the traces is at the time of 3 ms after the end of the 30 ms step. **G2**, Normalized cumulative release from P16–P19 synapses. The endpoint of the traces is at the time of 3 ms after the end of the 10 ms step. **H**, Summary for the number of SVs released by Dep3 ms and Dep30 ms in P9–P11 group and Dep1 ms and Dep10 ms in P16–P19 group. The numbers of fast-releasing SVs released by Dep30 ms and Dep10 ms are shown as fast pool in P9–P11 group and P16–P19 group, respectively. Data are presented as mean ± SEM.

Table 1. Summary of synaptic response and SV release rate from P9–P11 calyx of Held synapse

Parameter	Dep3 ms (mean ± SEM; n)	Dep30 ms (mean ± SEM; n)	p value (paired t test)
EPSC amplitude (nA)	15.5 ± 1.30 (9)	16.8 ± 1.36 (9)	> 0.05
Calcium charge (pC)	3.81 ± 0.29 (9)	32.2 ± 2.89 (9)	NA
10%–90% EPSC rise time (ms)	1.87 ± 0.08 (9)	2.23 ± 0.19 (9)	< 0.05
Synaptic delay (ms)	2.27 ± 0.11 (9)	2.43 ± 0.13 (9)	< 0.05
Vesicles released (vesicles)	1370 ± 157 (9)	2137 ± 306 (9)	< 0.01

NA, Not analyzed.

with 20 mM EGTA (see Fig. 6), refilling was not corrected because the RRP could not be depleted. The corrected cumulative release was fitted with double exponential function from the early onset of release to 3 ms after the end of the depolarization. The faster component in the fitting was considered as fast-releasing SV pool (fast pool); the slower component was considered as slow-releasing SV pool (slow pool).

Diffusion-reaction simulations of Ca²⁺. Using SDS-digested freeze-fracture replica immunogold labeling, we previously demonstrated that $Ca_v2.1$ channels are clustered at both young and old animals (Nakamura et al., 2015). Based on this finding, as well as experimental results estimating EGTA inhibition of AP-evoked release and the properties of endogenous fixed buffers, we used numerical simulations to establish that SVs are tightly coupled to the perimeter of VGCC clusters (Nakamura et al., 2015). The model proposed here also considers variable distances of SV from the edge of VGCC clusters but simulates SV release in response to voltage step depolarization rather than APs, and allows the possibility that SVs may be located at more distal sites.

Here we simulate the spatial and temporal profile of [Ca²⁺] following voltage step activation of VGCC located in clusters using the Java-based simulation environment D3D (DiGregorio et al., 2007; Nakamura et al., 2015). Ca²⁺ entry, diffusion, and binding with buffers were simulated by numerically integrating partial differential equations applying an explicit finite-element (Euler) method (DiGregorio et al., 1999), using experimentally constrained endogenous fixed buffer properties (Nakamura et al., 2015). Diffusion was allowed within a volume 0.8 (x) × 0.8 (y) × 1.0 (z) µm, containing a single Ca²⁺ entry site. The height (z) matches the thickness of the terminal (Sätzler et al., 2002), whereas the x and y dimensions correspond to the average nearest neighbor distance between VGCC clusters (Nakamura et al., 2015). The elemental simulation volume (voxels) was 10 × 10 × 10 nm used for finite difference calculations. The four x/y surfaces were set to reflect any diffusants, thus being mathematically equivalent to an infinitely extended synaptic surface of the calyx. The Ca²⁺ entry site was placed in the center of a single surface $(z = 0)$ bounding this volume. The entry site consisted of 24 channels placed in a grid manner separated by their nearest-neighbor distance of 20 nm (calculated from Nakamura et al., 2015). Similar nearest-neighbor distance was estimated using atomic force microscopy of 30 nm gold particles in the chick calyx preparation (Haydon et al., 1994). The time course of the Ca²⁺ entry was adopted directly from measured I_{Ca} traces (see Figs. 1B, 4B, 6E, and 7B), but scaled to match the amplitude of the single-channel current estimated from single-channel recordings at the calyx of Held and calibrated for 2 mM extracellular Ca²⁺ (0.15 pA) (Sheng et al., 2012). It should be noted that a similar value for single-channel current was determined for $Ca_v2.2$ channels in the chick ciliary ganglion (Weber et al., 2010). Because the open probability was estimated to be 0.5 at 0 mV (Sheng et al., 2012), we assumed all channels could eventually open during the step pulse, but accounted for the open probability by reducing the single-channel current by half (0.075 pA). For simulations in 1.2 mM Ca²⁺, the amplitude of this mean single VGCC current was scaled to 0.06 pA according to the ratio of measured I_{Ca} (1.2 mM vs 2 mM Ca²⁺). Model parameters were set to match experimental condition as often as possible: resting free [Ca²⁺] = 50 nM, Ca²⁺ diffusion coefficient (D_{Ca}^{2+}) = 220 µm²/s (Allbritton et al., 1992), endogenous fixed buffer (EFB) binding ratio = 40 (Helmchen et al., 1997), EFB concentration = 4 mM, EFB K_D = 100 µM, and an EFB forward binding rate of (k_{on}) = 1 × 10⁸/Msec (Nakamura et al., 2015). We included 650 µM free ATP in the simulation to match the expected free ATP concentration in our patch pipette (calculate using Max Chelator based on 4 mM

total Mg-ATP). The values for Ca²⁺ binding to ATP were as follows: $K_{D, Ca}$ = 200 µM, $k_{on, Ca}$ = 5 × 10⁸/Msec (Baylor and Hollingworth, 1998), D_{ATP} = 220 µm²/sec. The parameters for EGTA were as follows: $k_{on,}$ = 1.05 × 10⁷/Msec, K_D = 70 nM, D_{EGTA} = 220 µm²/sec (Nägerl et al., 2000). The time step was calculated according to a stability criterion, $h = (3 \times D \times dt)/\partial x^2$, where D is the diffusion coefficient of the fastest species and ∂x is the length of vertices of simulation voxels.

Release simulation and the estimation of SV distance. We recently found that AP-evoked release is best modeled by sensors located at the periphery of VGCC clusters (Nakamura et al., 2015). Therefore, to simulate vesicular transmitter release, we used 5-state model of Ca²⁺-dependent vesicle fusion of developing mice (Wang et al., 2008), integrated using a forward Euler numerical integration routine (IgorPro). SV release was then simulated from the modeled [Ca²⁺] (above) at various distances from the perimeter of VGCC clusters. The output of the release model is the probability that a single SV will be released as a function of time (single SV release rate), at a given location. Cumulative release rates were calculated from the integral of the single SV release rates. To estimate the distribution of SVs, we linearly combined different numbers of single SV release rates or their cumulative release rate for each simulation voxel, until the resulting summed release rate trace matched by eye both the experimental release rate and cumulative release rate. We did not time shift single SV release rates. The number of single SV release rate traces per location (simulation voxels) was taken to be the number of released SVs at a particular distance from the VGCC cluster. Contour lines were drawn using the implemented function of Igor. For simulation results, values are given as mean ± SD.

Results

The readily releasable pool at the functionally mature calyx of Held

To examine the RRP in the posthearing, functionally mature calyx (P16–P19), we used paired whole-cell voltage-clamp recordings of the calyx/MNTB synapse, which is amenable to presynaptic voltage clamp (Yang and Wang, 2006). To characterize the release kinetics, we delivered step depolarizations (steps) of variable duration to the presynaptic terminal to evoke transmitter release (Lee et al., 2012). First, we validated this protocol by estimating the RRP dynamics at the prehearing (P9–P11) calyces from mice. For steps 3 ms or longer, the EPSC amplitudes were similar (Fig. 1A1; Table 1), indicating a fast pool of SVs within the RRP, which depletes within 3 ms (Fig. 1B1,C). In addition, the slow decay of the EPSC evoked by a 30 ms step was comparable with a much longer step (50 ms), indicating that the 30 ms depolarization was sufficient to deplete the RRP (Fig. 1A1). Our results indicate that the peak of the EPSC evoked by a 3 ms step can be used to measure the fast pool, whereas the EPSC evoked by a 30 ms step can be used to measure the RRP in the P9–P11 calyx, as previously reported in rats (Lee et al., 2012).

However, in the P16–P19 calyx, we found that the 1 ms and all the subsequent longer step times resulted in similar peak EPSC amplitudes (Fig. 1A2,B2,C). Longer steps did not increase the peak ESPC amplitude, suggesting that the fast pool of SVs can be released in 1 ms. Analysis of the decay of the EPSCs, which is thought to be influenced by slowly releasing SVs in both P9–P11 and P16–P19 (Sakaba and Neher, 2001a, b, c; Wang et al., 2008), revealed that the 10 ms step was sufficient to release all SVs within the RRP, as longer step duration did not further extend the EPSC decay (Fig. 1A2). Additionally, EPSCs evoked by 1 and 10 ms steps exhibited similar 10%–90% rise time and synaptic delay (Table 2). Together, these results demonstrate that, at the P16–P19 calyx, there is an acceleration of SV release from the fast pool within the RRP and in the RRP compared with the P9–P11 calyx.

Table 2. Summary of synaptic response from different recording conditions at P16–P19 calyx of Held synapse[a]

Parameters	Conditions	Stimulation			Paired t test
		Dep1 ms (mean ± SEM; n)	Dep10 ms (mean ± SEM; n)	Dep50 ms (mean ± SEM; n)	p value (Dep1 ms vs Dep 10 ms)
EPSC amplitude (nA)	2 mM $[Ca^{2+}]_e$ and 0.5 mM $[EGTA]_i$ (a)	22.0 ± 2.40 (11)	21.00 ± 2.20 (11)	NA	$p > 0.05$
	2 mM $[Ca^{2+}]_e$ and 5 mM $[EGTA]_i$ (b)	21.0 ± 1.83 (13)	20.3 ± 1.73 (13)	NA	$p > 0.05$
	2 mM $[Ca^{2+}]_e$ and 20 mM $[EGTA]_i$ (c)	4.73 ± 1.03 (8)	5.28 ± 0.56 (8)	5.02 ± 0.48 (7)	$p > 0.05$ [1 ms vs 10 ms];
					$p > 0.05$ [1 ms vs 50 ms];
					$p > 0.05$ [10 ms vs 50 ms]
	1.2 mM $[Ca^{2+}]_e$ and 0.5 mM $[EGTA]_i$ (d)	17.1 ± 3.07 (9)	18.2 ± 3.33 (9)	NA	$p > 0.05$
Unpaired t test	Compare EGTA effect	$p > 0.05$, a versus b;	$p > 0.05$, a versus b;		
		$p < 0.0001$, a versus c	$p < 0.0001$, a versus c		
	Compare calcium effect	$p > 0.05$, a versus d	$p > 0.05$, a versus d		
Calcium influx charge (pC)	2 mM $[Ca^{2+}]_e$ and 0.5 mM $[EGTA]_i$ (a)	1.51 ± 0.11 (11)	11.2 ± 1.73 (11)	NA	NA
	2 mM $[Ca^{2+}]_e$ and 5 mM $[EGTA]_i$ (b)	1.66 ± 0.10 (13)	12.5 ± 0.69 (13)	NA	NA
	2 mM $[Ca^{2+}]_e$ and 20 mM $[EGTA]_i$ (c)	1.19 ± 0.17 (8)	9.62 ± 0.95 (8)	42.31 ± 4.32 (7)	NA
	1.2 mM $[Ca^{2+}]_e$ and 0.5 mM $[EGTA]_i$ (d)	1.21 ± 0.16 (9)	9.09 ± 0.88 (9)	NA	NA
Unpaired t test	Compare EGTA effect	$p > 0.05$, a versus b;	$p > 0.05$, a versus b;		
		$p > 0.05$, a versus c	$p > 0.05$, a versus c		
	Compare calcium effect	$p = 0.058$, a versus d	$p < 0.05$, a versus d		
10%–90% EPSC rise time (ms)	2 mM $[Ca^{2+}]_e$ and 0.5 mM $[EGTA]_i$ (a)	0.61 ± 0.02 (11)	0.60 ± 0.02 (11)	NA	$p > 0.05$
	2 mM $[Ca^{2+}]_e$ and 5 mM $[EGTA]_i$ (b)	0.65 ± 0.02 (13)	0.67 ± 0.03 (13)	NA	$p > 0.05$
	2 mM $[Ca^{2+}]_e$ and 20 mM $[EGTA]_i$ (c)	0.68 ± 0.02 (8)	1.34 ± 0.19 (8)	1.47 ± 0.18 (7)	$p < 0.05$ [1 ms vs 10 ms];
					$p < 0.05$ [1 ms vs 50 ms];
					$p > 0.05$ [10 ms vs 50 ms]
	1.2 mM $[Ca^{2+}]_e$ and 0.5 mM $[EGTA]_i$ (d)	0.66 ± 0.01 (9)	0.75 ± 0.03 (9)	NA	$p < 0.05$
Unpaired t test	Compare EGTA effect	$p > 0.05$, a versus b;	$p > 0.05$, a versus b;		
		$p < 0.05$, a versus c	$p < 0.001$, a versus c		
	Compare calcium effect	$p < 0.05$, a versus d	$p < 0.001$, a versus d		
Synaptic delay (ms)	2 mM $[Ca^{2+}]_e$ and 0.5 mM $[EGTA]_i$ (a)	1.02 ± 0.03 (11)	1.00 ± 0.02 (11)	NA	$p > 0.05$
	2 mM $[Ca^{2+}]_e$ and 5 mM $[EGTA]_i$ (b)	1.07 ± 0.04 (13)	1.05 ± 0.04 (13)	NA	$p > 0.05$
	2 mM $[Ca^{2+}]_e$ and 20 mM $[EGTA]_i$ (c)	1.34 ± 0.06 (8)	1.52 ± 0.12 (8)	1.49 ± 0.14 (7)	$p > 0.05$ [1 ms vs 10 ms];
					$p > 0.05$ [1 ms vs 50 ms];
					$p > 0.05$ [10 ms vs 50 ms]
	1.2 mM $[Ca^{2+}]_e$ and 0.5 mM $[EGTA]_i$ (d)	1.14 ± 0.03 (9)	1.13 ± 0.02 (9)	NA	$p > 0.05$
Unpaired t test	Compare EGTA effect	$p > 0.05$, a versus b;	$p > 0.05$, a versus b;		
		$p < 0.0001$, a versus c	$p < 0.0001$, a versus c		
	Compare calcium effect	$p < 0.01$, a versus d	$p < 0.001$, a versus d		

[a]Two-tailed unpaired t test was used to compare a versus b, a versus c; one-tailed unpaired t test was used to compare a versus d. NA, Not analyzed.

Quantitative analysis of the RRP at the functionally mature calyx

To more thoroughly analyze the contribution and amplitude of each pool, we deconvolved the EPSC to derive the release rate as a function of time (Neher and Sakaba, 2001b; Wang et al., 2008) (for detailed explanation, see Material and Methods) for both P9–P11 and P16–P19 calyces, which we will from here on refer to as release rate. Deconvolution analysis revealed that the peak release rates were dramatically increased in P16–P19 calyces compared with P9–P11 calyces (1541 ± 155 SV/ms; $n = 11$ vs 522 ± 511 SV/ms; $n = 9$; $p < 0.0001$) (Fig. 1D), similar to the developmental acceleration of release in response to APs (Taschenberger et al., 2005; Wang et al., 2008; Kochubey et al., 2009). Furthermore, analysis of the release rate for the 10 ms step demonstrated a clear appearance of a slowly released component in P16–P19 calyces, although this slow component was much faster than the slow component in P9–P11 calyces (Fig. 1F).

To determine the RRP size, we integrated the release rate for the 30 ms step from P9–P11 calyces and 10 ms step from P16–P19 (Fig. 1D), and corrected for ongoing replenishment during the depolarization (Neher and Sakaba, 2001b). Analysis of the cumulative release rates revealed that RRP size was increased from P9–P11

to P16–P19 by ~30% (2137 ± 306 SVs; $n = 9$ vs 2714 ± 247 SVs; $n = 11$) (Tables 1 and 3). This developmental increase in the RRP size was not due to the correction for ongoing replenishment as the uncorrected pool sizes in P16–P19 calyces (2818 ± 258 SVs; $n = 11$) were also larger than in P9–P11 calyces (2396 ± 342 SVs; $n = 9$).

We also integrated the peak release rates of the 1 and 3 ms steps to determine the putative fast pool size in both age groups. Fast pools were also increased from P9–P11 (1370 ± 158 SVs; $n = 9$) to P16–P19 (1759 ± 183 SVs; $n = 11$) (Fig. 1E1,E2,H). We estimated the relative fraction of the fast pool size (3 or 1 ms) by dividing its integrated vesicular release by the total RRP size (corrected 30 or 10 ms). The fast pool occupies ~64% of total RRP in P9–P11 calyces in agreement with previous reports (Chen et al., 2013), and similarly, it occupies ~65% in P16–P19 calyces. To corroborate our definition of fast and slow pools in P16–P19 calyces, we fit the cumulative release rate with a double exponential function (Sakaba and Neher, 2001c). Analysis revealed that the RRP was depleted with 2 distinct time constants (0.87 ± 0.04 ms vs 4.18 ± 0.24 ms; $n = 11$), comprised of 1701 ± 235 fast SVs ($n = 11$) and 1011 ± 147 slow SVs ($n = 11$), which closely matched the sizes determined from 1 and 10 ms steps, respectively. This held true for our measurements at P9–P11 calyces as previously reported (Chen et al., 2013) and matched the

Table 3. Summary of SV release rates at P16–P19 calyx of Held synapse under different recording conditions[a]

Parameters	Conditions	Stimulation			Paired t test
		Dep1 ms (mean ± SEM; n)	Dep10 ms (mean ± SEM; n)	Dep50 ms (mean ± SEM; n)	p value (Dep1 ms vs Dep10 ms)
Peak release rate (vesicles/ms)	2 mM $[Ca^{2+}]_e$ and 0.5 mM $[EGTA]_i$ (a)	1605 ± 160 (11)	1541 ± 154 (11)	NA	$p > 0.05$
	2 mM $[Ca^{2+}]_e$ and 5 mM $[EGTA]_i$ (b)	1559 ± 140 (13)	1502 ± 138 (13)	NA	$p > 0.05$
	2 mM $[Ca^{2+}]_e$ and 20 mM $[EGTA]_i$ (c)	335 ± 73 (8)	313 ± 51 (8)	260 ± 43 (7)	$p > 0.05$ [1 ms vs 10 ms]; $p > 0.05$ [1 ms vs 50 ms]; $p > 0.05$ [10 ms vs 50 ms]
	1.2 mM $[Ca^{2+}]_e$ and 0.5 mM $[EGTA]_i$ (d)	1123 ± 215 (8)	1179 ± 240 (8)	NA	$p > 0.05$
Unpaired t test	Compared EGTA effect	$p > 0.05$, a versus b; $p < 0.0001$, a versus c	$p > 0.05$, a versus b; $p < 0.0001$, a versus c	$p > 0.05$, a versus b; $p < 0.0001$, a versus c	
	Compared calcium effect	$p > 0.05$, a versus d	$p > 0.05$, a versus d	$p < 0.05$, a versus d	
Vesicles released (vesicles)	2 mM $[Ca^{2+}]_e$ and 0.5 mM $[EGTA]_i$ (a)	1759 ± 183 (11)	2714 ± 247 (11)	NA	NA
	2 mM $[Ca^{2+}]_e$ and 5 mM $[EGTA]_i$ (b)	1769 ± 181 (13)	3031 ± 295 (13)	NA	NA
	2 mM $[Ca^{2+}]_e$ and 20 mM $[EGTA]_i$ (c)	438 ± 93 (8)	1204 ± 124 (8)	1748 ± 176 (7)	$p < 0.0001$ [1 ms vs 10 ms]; $p < 0.0001$ [1 ms vs 50 ms]; $p < 0.001$ [10 ms vs 50 ms]
	1.2 mM $[Ca^{2+}]_e$ and 0.5 mM $[EGTA]_i$ (d)	1188 ± 223 (8)	2635 ± 530 (8)	NA	NA
Unpaired t test	Compared EGTA effect	$p > 0.05$, a versus b; $p < 0.0001$, a versus c	$p > 0.05$, a versus b; $p < 0.0001$, a versus c		
	Compared calcium effect	$p < 0.05$, a versus d	$p > 0.05$, a versus d		

[a]Two-tailed unpaired t test was used to compare a versus b, a versus c; one-tailed unpaired t test was used to compare a versus d. NA, Not analyzed.

fast pool size from the 3 ms step (Table 1). Comparison of the two time constants between P16–P19 and P9–P11 revealed that the fast and slow components become accelerated by ~2.5-fold and 4-fold, respectively. This acceleration in the P16–P19 calyx was also reflected in the normalized cumulative release curves (Fig. 1G). Together, our 1 and 10 ms step protocol can be used to estimate size of the fast pool and total RRP (fast and slow pools), respectively, in the P16–P19 calyx. More importantly, we demonstrate the existence of a slow pool of SVs within the RRP in the functionally mature calyx.

Simulations of RRP dynamics reveal that shortening the Ca²⁺ sensor distance to VGCCs reproduces the developmental changes in release kinetics of the RRP

The origin of fast and slow release components could be either different Ca^{2+} sensitivities of SVs (Wolfel et al., 2007; Schneggenburger et al., 2012) or different SV positions (Meinrenken et al., 2002; Wadel et al., 2007; Neher and Sakaba, 2008). To determine whether SV position relative to VGCCs could account for the fast and slow components of release, we first performed 3D reaction–diffusion simulations (DiGregorio et al., 1999; Nielsen et al., 2004) of the calyx terminal $[Ca^{2+}]$ using a recently established VGCC cluster perimeter release model that accurately predicts developmental changes in AP-evoked release (Nakamura et al., 2015). However, in this instance, we simulated the spatiotemporal profile $[Ca^{2+}]$ for step depolarization-induced activation of many VGCCs distributed in a tight cluster (Fig. 2A). The VGCC density (20 nm nearest neighbor distance) and number (24 VGCCs) were set according to average values obtained from the EM of SDS-freeze-fracture replica immunogold labeled samples (Nakamura et al., 2015). The endogenous Ca^{2+} buffer properties were also determined from Ca^{2+} imaging experiments (Nakamura et al., 2015). Simulation of the intracellular $[Ca^{2+}]$ in the proximity of VGCCs reached 100 μM within the first 1 ms of the step, then slowly increased to 120 μM by the end of the 10 ms pulse (Fig. 2B). This lack of increase in peak amplitude, plus a steep spatial dependence (Fig. 2C,D), argues that a standing $[Ca^{2+}]$ gradient is present and is nearly at steady state by the end

of the 10 ms depolarization step (i.e., not changing their spatial extent, despite longer durations of Ca^{2+} entry).

Next, we estimated SV release rates at particular locations (i.e., individual simulation voxels) with a 5-state release model for functionally mature mice (Wang et al., 2008), triggered by the simulated $[Ca^{2+}]$ time course at that voxel. Our simulations revealed that the maximum release rate decreased more steeply than the $[Ca^{2+}]$ at increasing distance from the VGCC cluster (Fig. 2C). This effect is clearly illustrated in a plot of the release probability (integral of release rate) versus sensor distance from the periphery of VGCC cluster (Fig. 2D). In response to a 1 ms step, the SV release probability was one within 20 nm and then fell sharply with increasing distance from the cluster (Fig. 2D). In response to a 10 ms step, the SV release probability was one up to 60 nm. We found that the distance that corresponded to a 50% release probability was 31 nm for 1 ms step and was 119 nm for the 10 ms step, respectively. Furthermore, the simulations show that longer steps more efficiently triggers SV release at further distances (Fig. 2D). To examine which sensor locations reproduced a release time course comparable with measured release rates, we normalized the release rate and cumulative release (Fig. 2E,F). The time course of release became slower at longer distance (Fig. 2G), and no single location could reproduce the fast and slow release components (compare with Fig. 2E, inset, thick gray trace).

Therefore, we considered the possibility that a distribution of SV locations might better predict experimental release rates. To estimate possible spatial distributions, we linearly combined multiples of single SV release rates and cumulative release rates, calculated for individual simulation voxels (without time shifting), until the summed release time course and summed cumulative release rate matched the experimental release rate and cumulative release rate, respectively, of the whole calyx estimated for 1 and 10 ms steps (Fig. 3A,B). The number value of the release rate (or cumulative release rate) for each location was then transformed directly into a single distribution of the number value of SVs as a function of location (Fig. 3C). For the 1 ms step, the majority of SVs contributing to release were estimated to be within 20 nm of the cluster perimeter (16 ± 8 nm). However,
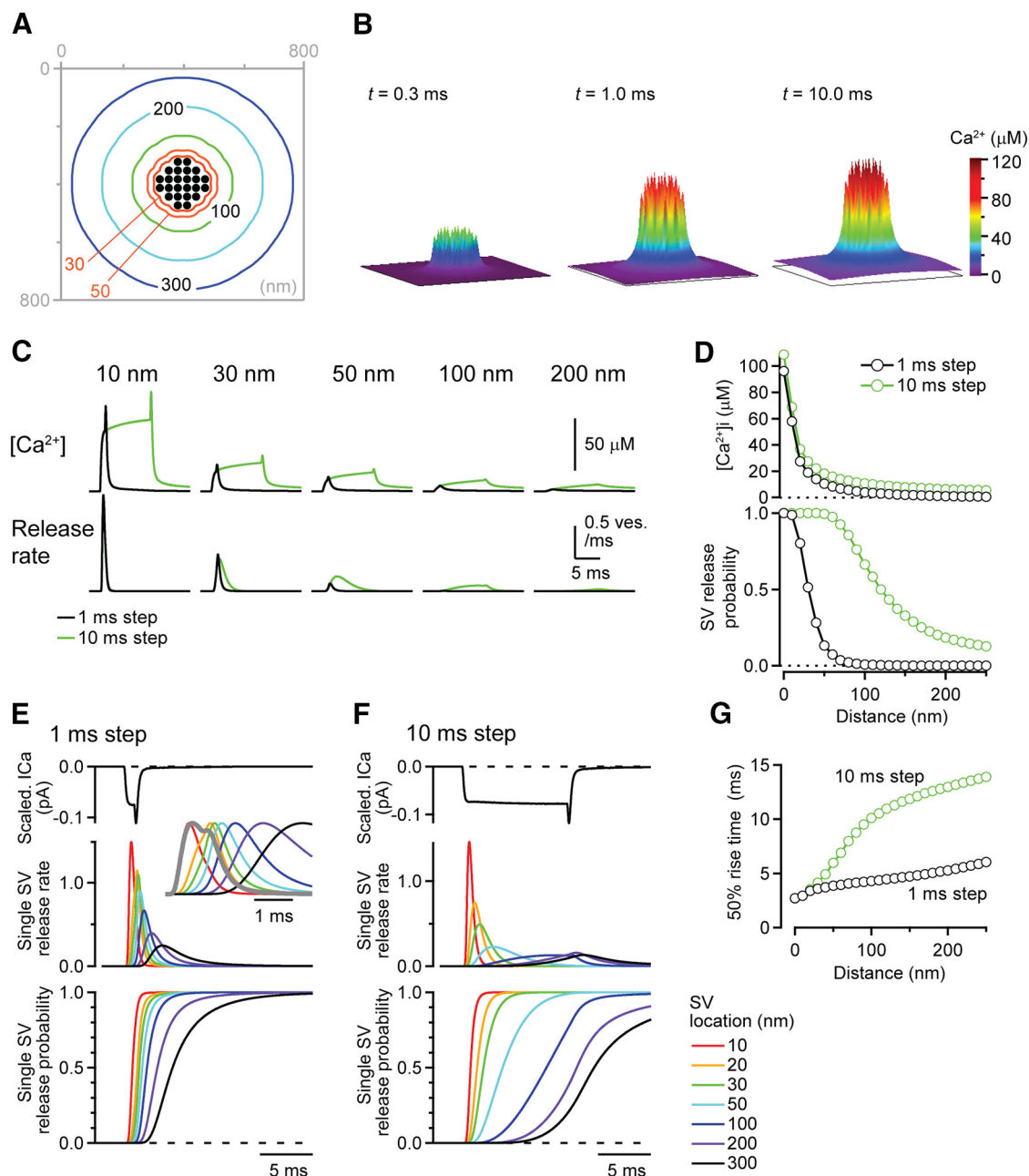
Figure 2. Numerical simulations for Ca^{2+} diffusion and release time course in functional mature calyces. **A**, Schematic diagram showing VGCC locations at the synaptic surface. A total of 24 VGCCs are placed at the center of simulation volume (nearest neighbor distance = 20 nm). Lines indicate the distance from the nearest VGCC. **B**, Spatial distribution of local [Ca^{2+}] formed around a VGCC cluster in response to 10 ms steps. [EGTA]$_i$ is 0.5 mM. **C**, Simulated time course of [Ca^{2+}] (top) and corresponding release rate (bottom) at various distances from the nearest VGCC (i.e., cluster perimeter) in response to 1 ms (black) and 10 ms (green) step durations. **D**, The [Ca^{2+}] (measured at the end of step, just before the tail component) and release probability were plotted against the distance from the nearest VGCC. **E**, Top, Experimental I$_{Ca}$ trace evoked by a 1 ms step, which was scaled such that the current at the end of the step equaled one-half the single-channel current (to account for 0.5 open probability) and then used to define the Ca^{2+} entry through a single channel. Middle, Simulated single SV release rate, in response to scaled I$_{Ca}$, for various distances from the nearest VGCC. Inset, The same traces, but normalized. Thick gray trace represents the release rate estimated from deconvolution of measured EPSC. Bottom, Cumulative single SV release rate. **F**, Same as **E**, but simulations were performed with a I$_{Ca}$ evoked by 10 ms steps. **G**, Plot of the 50% rise time of the cumulative release (measured from the onset of Ca^{2+} influx) versus distance.

release rates in response to the 10 ms step depolarization required additional SVs to be positioned at longer distances from the cluster perimeter (∼20–100 nm). To elucidate the spatial distribution of only those SVs corresponding to the slowly releasing pool of SVs with the RRP, we subtracted the SV distribution for 1 ms step from that for 10 ms step and determined that the mean distance of slowly releasable SVs was 53 ± 21 nm.

The spatial distribution of SVs within the RRP in P9–P11 calyces was estimated using simulations of Ca^{2+} entry during 3

and 30 ms step depolarization (Fig. 1B1) and calculated release using 5-state release model for P9–P11 mice (Wang et al., 2008). Release rate time courses were well fit by a linear combination of simulated single SV release rates from different locations (Fig. 3D,E). SV locations corresponding to both the fast and slow release components were shifted to longer distances in P9–P11 calyces (Fig. 3F), giving a mean distance of 56 ± 38 nm for the fast pool and 135 ± 80 nm for the slow pool. More importantly, these simulations suggest that the RRP release kinetics
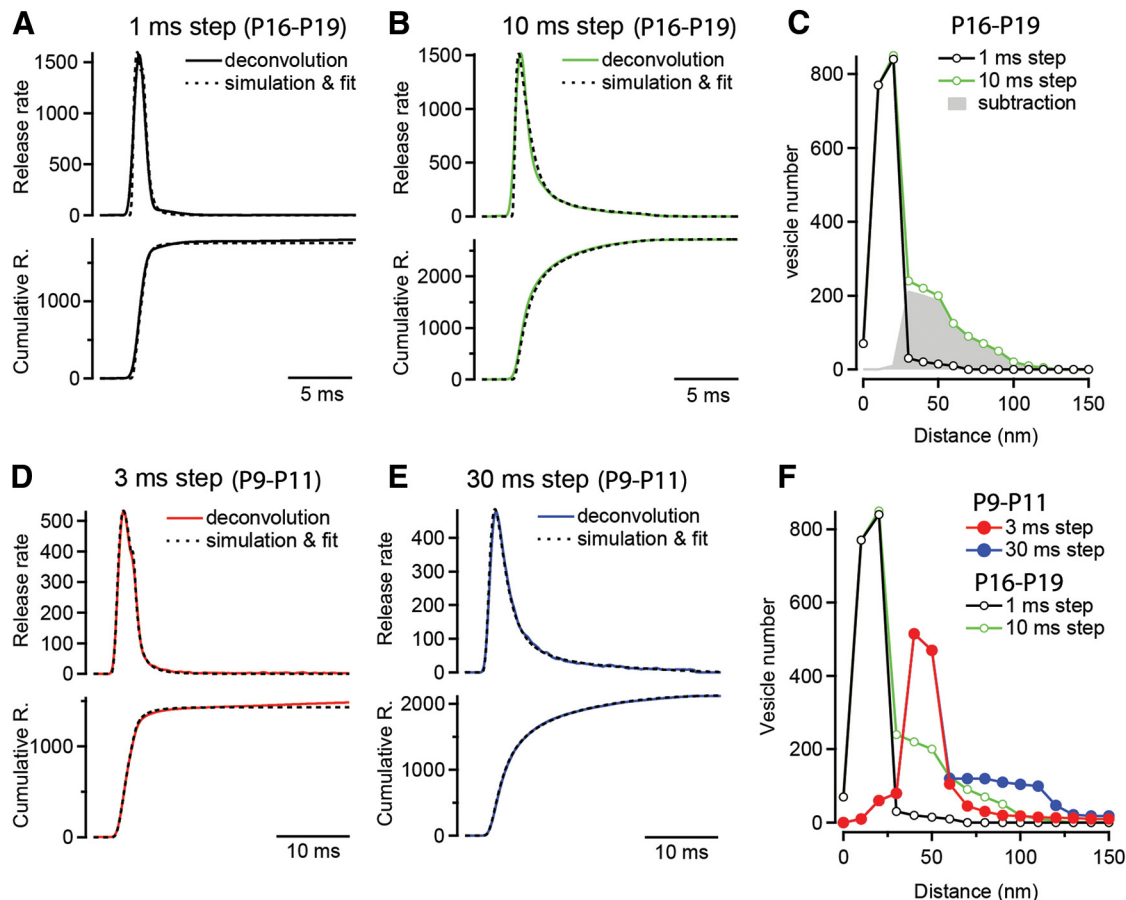
Figure 3. Estimating pool locations using the combination of deconvolution and simulation at P9 –P11 and P16 –P19 calyces. ***A***, Experimental release rate (top) and cumulative release (bottom) representing the population average from P16 –P19 calyces for 1 ms step. Traces were fit with a linear combination of simulated single SV release rate and cumulative release rates, respectively (dashed line). ***B***, Same as ***A***, but for 10 ms step. ***C***, Spatial distributions of released SVs that was used to fit traces in ***A*** and ***B***; distribution for 1 and 10 ms steps. Gray area represents the subtraction between the two distributions. ***D***, Same as ***A***, but for P9 –P11 calyces and for a 3 ms step. ***E***, Same as ***D***, but for 30 ms step. ***F***, Fitted spatial distributions of SVs as in ***C***, but for P9 –P11 calyces, and for comparison P16 –P19, for different steps.

in both the P9–P11 and P16–P19 calyces can be determined exclusively by a heterogeneous distribution of distances between SVs and VGCC cluster perimeters.

We would like to stress the reaction–diffusion and release simulations are based on key experimentally measured parameters, such as single-channel current at the calyx of Held (Sheng et al., 2012) and VGCC localization (Nakamura et al., 2015). Although we did not consider stochastic channel opening here, the spatial averaging by diffusion and sensor binging over the long step depolarization suggests that deterministic simulations are an appropriate simplification (Klingauf and Neher, 1997). However, it is important to note the choice of release model can be important for precise distance estimates because we found that, in young animal simulations, an allosteric binding model (Lou et al., 2005) predicted longer VGCC-SV distance (60% increase) for the slow pool (data not shown). Unfortunately, an allosteric model for older animals does not exist.

EGTA (5 mM) has no significant effects on the release kinetics of the RRP in the functionally mature calyx
Based on our simulations, both SV pools in the functionally mature calyx become more tightly coupled to VGCCs, with the fast pool SV distances matching those proposed for SVs released by APs (Fedchyshyn and Wang, 2005; Wang et al., 2009; Nakamura et al., 2015). Therefore, we hypothesized that the release rates of the fast and slow

pool in the RRP should be differentially sensitive to additions of high concentrations of the slow exogenous Ca²⁺ chelator, EGTA, as EGTA has been extensively used as an indirect estimate of VGCC to SV distances (Adler et al., 1991; Eggermann et al., 2011). In P9–P11 calyces, increasing the EGTA concentration ([EGTA]$_i$) from 0.5 to 5 mM, slowed down the release kinetics of the RRP and resulted in incomplete depletion of the RRP (Sakaba and Neher, 2001c), but in P16–P19 calyces, increasing [EGTA]$_i$ to 5 mM did not affect the EPSC amplitude, rise time, or synaptic delays (Fig. 4B; Table 2). The 1 ms and the subsequent longer step durations also resulted in similar peak EPSC amplitude, rise time, and synaptic delay (Table 2), suggesting that 1 ms also depletes the fast pool in the presence of 5 mM EGTA. For durations >10 ms, we observed similar EPSC decays, consistent with RRP depletion by 10 ms, similar to control condition (Fig. 4A). In addition, 5 mM EGTA resulted in no change in the peak release rates, RRP size, or time the constants of release from the slow pool release (Fig. 4C1,D1; Table 3). Furthermore, the contribution of the fast pool to the RRP (SVs released by 1 ms/ SVs released by 10 ms) was also similar (Fig. 4E,F). However, 5 mM EGTA slightly slowed the time constants of the fast pool (1.05 ± 0.05 ms; n = 13; 5 mM EGTA vs 0.87 ± 0.04 ms; n = 11; 0.5 mM EGTA; $p < 0.05$) (Table 4).

To estimate SV locations that would reproduce measured release rates, [Ca²⁺] changes were simulated in the presence of 5 mM EGTA (Fig. 5A). The 5 mM EGTA had no significant effect on
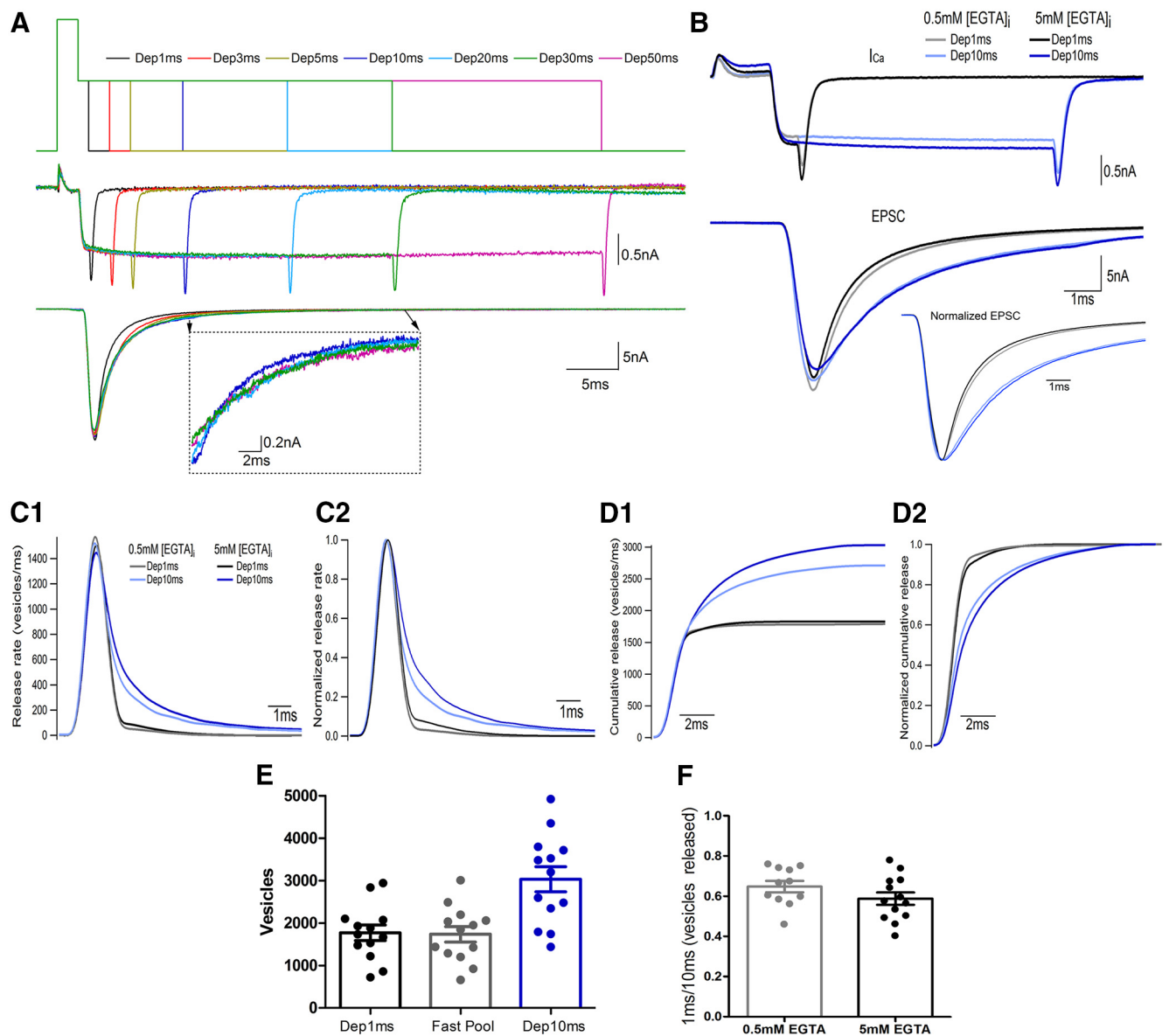
Figure 4. The 5 mM EGTA does not attenuate the fast synaptic transmission at the P16–P19 calyx of Held. *A*, Stimulation protocol (top) and resulting presynaptic I_{Ca} (middle) and EPSCs (bottom). Dashed line box represents a magnified view of the decaying EPSCs. *B*, Average traces of I_{Ca} (top) and corresponding average traces of EPSCs (bottom) from 0.5 and 5 mM EGTA groups. Inset, Normalized EPSCs. *C*, Average release rate (*C1*) and normalized peak release rate (*C2*). *D*, Average cumulative release (*D1*) and normalized cumulative release (*D2*) from 0.5 mM EGTA group and 5 mM EGTA group. *E*, Summary for number of SVs released by Dep1 ms and Dep10 ms in 5 mM EGTA group. The numbers of fast-releasing SVs released by Dep10 ms are shown as fast pool. *F*, Comparison of the ratio of number of SVs released by Dep1 ms to Dep10 ms in 0.5 and 5 mM EGTA group. *E*, *F*, Data are presented as mean ± SEM.

Table 4. Time constants of RRP release in P16–P19 calyx of Held

Parameters	Conditions			Unpaired *t* test (*p* value)
	2 mM $[Ca^{2+}]_e$ and 0.5 mM $[EGTA]_i$ (a)	2 mM $[Ca^{2+}]_e$ and 5 mM $[EGTA]i$ (b)	1.2 mM $[Ca^{2+}]_e$ and 0.5 mM $[EGTA]_i$ (c)	
Tau fast (mean ± SEM; ms)	0.87 ± 0.04	1.05 ± 0.05	1.17 ± 0.10	$p < 0.05$, a versus b
n	11	13	8	$p < 0.01$, a versus c
Tau slow (mean ± SEM; ms)	4.18 ± 0.24	3.81 ± 0.15	4.30 ± 0.32	$p > 0.05$, a versus b
n	11	13	8	$p > 0.05$, a versus c

the peak $[Ca^{2+}]$ induced by 1 ms step but decreased peak $[Ca^{2+}]$ and release probability induced by 10 ms step (Fig. 5*B*,*C*). The inhibition of the $[Ca^{2+}]$ increased with increasing distance from the cluster, reducing the calculated release probability preferentially at distal locations (Fig. 5*C*). Interestingly, the $[Ca^{2+}]$ at 200 nm remained close to resting levels in the presence of 5 mM EGTA, suggesting no crosstalk between Ca^{2+} entry sites. When

release rates time courses were fit with the sum of simulated single SV release rates (Fig. 5*D*,*E*), as described above (Fig. 3*D*,*E*), the estimated SV distances in 5 mM EGTA were similar to those in 0.5 mM EGTA (Fig. 5*F*). Together, a 10-fold increase of $[EGTA]_i$ did not change the RRP release kinetics or the estimated distance between SVs and VGCC in the P16–P19 calyx, suggesting that 5 mM EGTA is not capable of blocking release at distances <100
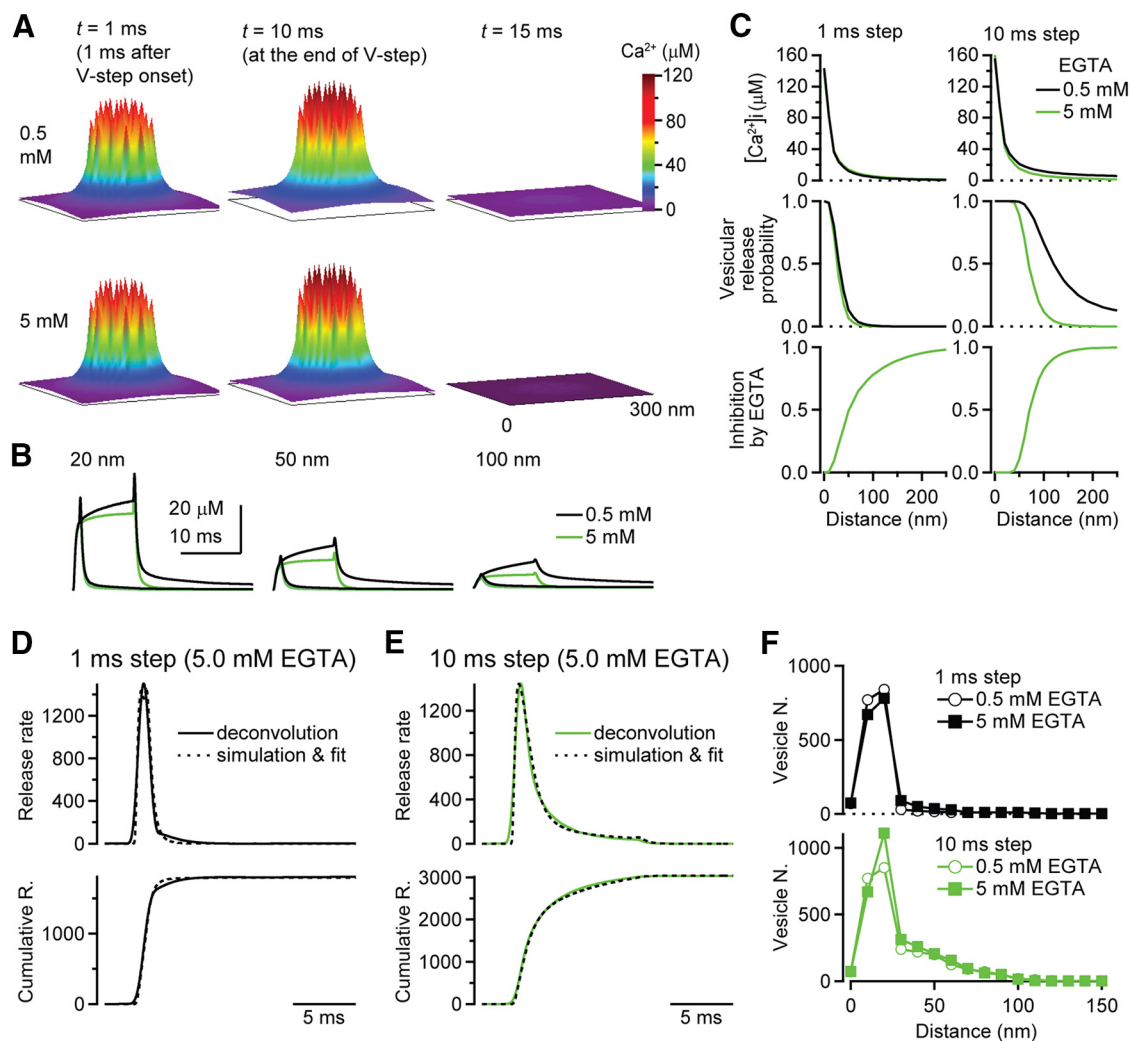
Figure 5. The effect of 5 mM EGTA on estimated SV locations. ***A***, Spatial distribution of local $[Ca^{2+}]$ formed around a VGCC cluster at 1 ms (left), 10 ms (middle), and 15 ms (right) after the onset of 10 ms step in the presence of 0.5 mM (top) and 5 mM (bottom) EGTA. ***B***, Time course of $[Ca^{2+}]$ at various distances from the nearest VGCC in response to 1 ms (black) and 10 ms (green) steps. ***C***, The amplitude of steady-state $[Ca^{2+}]$ (top), release probability (middle), and the inhibition of vesicular release probability by 5 mM EGTA (bottom) was plotted against the distance from the nearest VGCC. ***D***, Deconvolution traces in P16 –P19 calyces for 1 ms steps in the presence of 5 mM EGTA were fit with simulated single vesicle release and cumulative release rates. ***E***, Same as ***D***, but for 10 ms. ***F***, Spatial distributions of SVs released in 0.5 and 5 mM EGTA.

nm. Because the 5 mM EGTA simulations predict a dramatically reduced $[Ca^{2+}]$ between VGCC clusters, but did not affect the slow release component, we conclude that Ca^{2+} domains around VGCC clusters, rather than global $[Ca^{2+}]$, drives release of both close (10–20 nm) and distal (20–100 nm)-coupled vesicles.

EGTA (20 mM) inhibits release of synaptic vesicles from the slow pool
Because 5 mM EGTA was unable to selectively inhibit the release of SVs located distally from the VGCC cluster, we hypothesized that this $[EGTA]_i$ might not be sufficient. To test this theoretically, we performed simulation of $[Ca^{2+}]$ with 20 mM EGTA using I_{Ca} traces in the presence of 0.5 mM EGTA (Fig. 1B). We simulated the spatiotemporal profile of $[Ca^{2+}]$ in response to step depolarization in the presence of 20 mM EGTA and then predicted release from the locations estimated from 0.5 mM EGTA experiments (Fig. 3C). Our simulations revealed that, in contrast to 5 mM EGTA, 20 mM EGTA caused a decrease of the steady-state $[Ca^{2+}]$ both for 1 and 10 ms step with what was progressively larger for increasing distance from the cluster perimeter (Fig. 6A, B). Correspondingly, the magnitude of inhibi-

tion of release by 20 mM EGTA, relative to 0.5 mM EGTA, was larger at longer distances (Fig. 6C). Finally, the predicted the number of releasing SVs at various distances from VGCC cluster is shown in Figure 6D, indicating that, for the 10 ms step simulation, 20 mM EGTA inhibited release of SVs located >50 nm from the perimeter of VGCC clusters.

To test these predictions, we performed paired recordings with 20 mM EGTA in our presynaptic patch pipette (Fig. 6E). The higher $[EGTA]_i$ resulted in a significant reduction of the EPSC amplitudes compared with 0.5 mM EGTA (4.7 ± 1.0 nA; $n = 8$ vs 22.0 ± 2.4; $n = 11$, $p < 0.0001$; Table 2). In addition, we observed a reduction in the presynaptic I_{Ca} (Table 2). Unlike in the presence of 0.5 or 5 mM EGTA, increasing step durations evoked EPSCs with increasing decay times for steps up to 50 ms long, indicating that the RRP was not depleted by 10 ms in the presence of 20 mM EGTA (Fig. 6E, F). Further evidence of incomplete RRP depletion was an appearance of a hump during the decay of the EPSC, which corresponded to the Ca^{2+} tail current-induced release.

Deconvolution analysis demonstrated significant reduction in peak release rates (Fig. 6G; Table 3). Normalization of the
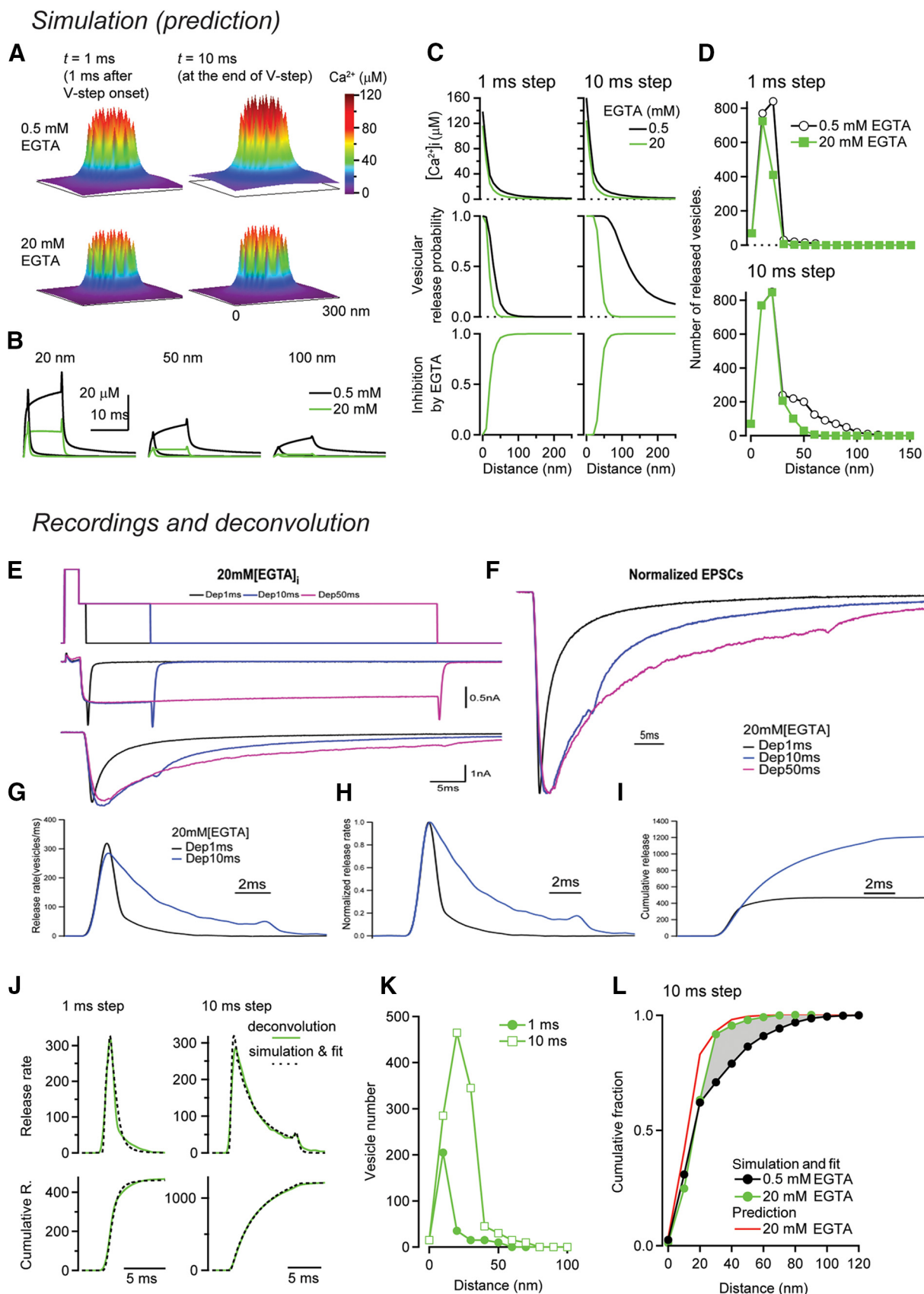
Figure 6. The 20 mM EGTA results in incomplete depletion of the RRP and reduction of release from distal SVs in the P16–P19 calyx of Held. **A**, Simulated spatial distribution of local [Ca²⁺] around a VGCC cluster in response to 1 ms step (left) and 10 ms step (right) in the presence of 0.5 mM (top) and 20 mM (bottom) EGTA. For both simulations, we used I_Ca template recorded in 0.5 mM EGTA. **B**, Simulated time course of [Ca²⁺] (top) and corresponding release rate (bottom) traces at various distances for 1 ms (black) and 10 ms (green) steps. **C**, The simulated steady-state [Ca²⁺] (top), release probability (middle), and the inhibition of vesicular release probability by 20 mM EGTA (bottom). **D**, Simulations using the spatial distribution of released (*Figure legend continues.*)

release rates revealed that 20 mM EGTA resulted in a dramatic slowdown in the SV release (Fig. 6H), as might be expected for a competition between the Ca^{2+} sensor with the high $[EGTA]_i$. Integration of the release rates revealed reductions in the release of both fast and slow SVs in the presence of 20 mM EGTA(Fig. 6I; Table 3). Furthermore, the RRP could not be depleted with a 50 ms step (1748 ± 176 SVs; $n = 7$; 20 mM EGTA 50 ms step vs 2714 ± 247 SVs; $n = 11$; 0.5 mM EGTA 10 ms step).

To estimate the SV locations in these experiments, we simulated the $[Ca^{2+}]$ and release using I_{Ca} waveform recorded in the presence of 20 mM EGTA (Fig. 6E). Simulations and fits of the measured release rates (Fig. 6J) revealed that SVs >50 nm were not necessary to reproduce release rates in response to the 10 ms steps (Fig. 6K). To compare the predicted vesicular release locations (Fig. 6D) with those estimated from fits to the deconvolution traces (Fig. 6K), we normalized and superimposed the cumulative spatial distributions of SVs (Fig. 6L), which were similar. Thus, our experimental and simulated results demonstrate that increasing $[EGTA]_i$ to 20 mM could sufficiently compete with SV release, thus preventing RRP depletion for 10 ms depolarization steps. Moreover, the SVs located >50 nm from the perimeter of the VGCC cluster were preferentially inhibited, as would be expected for the slow on-rate Ca^{2+} buffer, EGTA. Finally, these findings support the hypothesis that distally coupled SVs account for the slowly releasing pool in low EGTA conditions.

Lowering the external Ca^{2+} concentration selectively affects fast pool of the RRP

It has been demonstrated that the *in vivo* release characteristics of the functionally mature calyx can be mimicked by lowering external Ca^{2+} concentration ($[Ca^{2+}]_{ext}$) to 1.2 mM (Lorteije et al., 2009). In addition, lowered $[Ca^{2+}]_{ext}$ dramatically impacts the AP-evoked EPSC amplitude, suggesting that the release probability of SVs in the fast pool is affected (Neher and Sakaba, 2008). Using 1 ms steps, we found that the total entry of Ca^{2+} charge was reduced by 20% in the 1.2 mM Ca^{2+} (Table 2), which resulted in a reduction of EPSC amplitudes by ~20%. Our paired recording revealed that, although the EPSC amplitudes did not increase for step durations >1 ms, the decay continued to increase for durations up to 10 ms (Fig. 7A). However, at the end of 10 ms step, the decay of the EPSCs was similar in both $[Ca^{2+}]_{ext}$ (Fig. 7B), indicating that the 10 ms step is sufficient to release the total RRP in 1.2 mM Ca^{2+}. The 10%–90% rise time of the EPSC between 10 and 1 ms pulse was slower in 1.2 mM Ca^{2+} (0.75 ± 0.03 ms; $n = 9$ vs 0.66 ± 0.01; $n = 9$; $p < 0.05$) (Fig. 7B; Table 2).

←

(*Figure legend continued.*)   SV from 0.5 mM EGTA (Fig. 6C) predict that 20 mM EGTA (green) preferentially blocks release from distal vesicles. **E**, Presynaptic stimulation protocol (top), the presynaptic holding potential was depolarized to 0 mV gradually for 1 ms, 10 ms, and 50 ms. The stimulation protocol and the related responses are labeled as Dep1 ms, Dep10 ms, and Dep50 ms, respectively. Middle, Resulting presynaptic I_{Ca} values. Bottom, Corresponding EPSCs. Average traces for 1 and 10 ms ($n = 8$) and for 50 ms ($n = 7$) steps. **F**, Normalized EPSCs at 1, 10, and 50 ms depolarizations. **G**, Deconvolved release rates. **H**, Normalized values. **I**, Their integrated release rates to determine total SVs releases with Dep1 ms and 10 ms. **J**, Experimental release rates and cumulative release from P16–P19 calyces and their fit with linearly combined single vesicle release rate and cumulative release rate (dashed line), simulated with 20 mM EGTA. The Ca^{2+} entry was based on template I_{Ca} traces recorded in the presence of 20 mM EGTA (Fig. 6E) and with a single-channel conductance scaled by the ratio of whole terminal I_{Ca} amplitudes in recordings with 0.5 versus 20 mM EGTA. **K**, Spatial distributions of SVs released in response to 1 and 10 ms steps in the experiment with 20 mM EGTA. **L**, Cumulative histogram for the spatial distribution of vesicular release for the prediction (red, 20 mM EGTA) and the estimation from the fit of the deconvolution-derived cumulative release rates.

Deconvolution analysis revealed that the peak release rates were similar between 1 and 10 ms step durations; however, 1.2 mM Ca^{2+} reduced peak release rates by 30% compared with 2 mM Ca^{2+} (Fig. 7C1; Table 3). Normalization of the peak release rates demonstrate a slight slowdown in time to peak, although there was a significant increase in the proportion of delayed (slow) component compared with experiments performed in 2 mM Ca^{2+} (Fig. 7D2). The total RRP size in 1.2 mM Ca^{2+} was similar to 2 mM (2635 ± 530 SVs; $n = 8$ vs 2714 ± 247 SVs; $n = 11$) (Fig. 7D1,E; Table 3), although there was a significant decrease in the total number of SVs released by the 1 ms pulse (1188 ± 223 SVs; $n = 8$ vs 1759 ± 183 SVs; $n = 11$, $p < 0.05$) (Fig. 7E). This was in line with our results obtained with the double exponential fit of the integrated release rates demonstrating a significant slowdown in the release of the fast pool (1.17 ± 0.01 ms; $n = 8$ vs 0.87 ± 0.04 ms; $n = 11$, $p < 0.001$), but no change in the rate of release of the slow (4.30 ± 0.32 ms; $n = 8$ vs 4.18 ± 0.24 ms; $n = 11$) (Fig. 7D2; Table 4). Furthermore, the contribution of the fast pool to the RRP in 1.2 mM Ca^{2+} was smaller than that in 2 mM Ca^{2+} (0.45 ± 0.02; $n = 8$ vs 0.65 ± 0.03; $n = 11$; $p < 0.001$) (Fig. 7E,F). These data indicate that lowering $[Ca^{2+}]_{ext}$ did not alter the size of the RRP but slowed only the fast pool release rates, consistent with the intracellular Ca^{2+} concentration dependence of release rate (Bollmann et al., 2000; Schneggenburger and Neher, 2000).

We next used $[Ca^{2+}]$ and release simulations in which the single VGCC current was reduced (see Materials and Methods) to predict vesicle locations of the experiments performed in 1.2 mM Ca^{2+} (Fig. 7G–I). The 1 ms step simulations resulted in fewer released SVs from the fast pool only, but a similar distribution in the distances of fast released SVs, compared with 2 mM Ca^{2+} (14 ± 5 nm) (Fig. 7G,I). The 10 ms step simulations, on the other hand, resulted in similar number and distribution of released SVs (Fig. 7H,I). Subtraction of the 1 ms from the 10 ms step also revealed a similar spatial distribution of the slowly releasing SVs (37 ± 21 nm). The decrease in the release fraction during 1 ms steps in low $[Ca^{2+}]_{ext}$ is due to the smaller single-channel current that, even with clustered VGCCs, does not achieve a high enough release probability to deplete the fast pool. However, the 10 ms step duration is sufficient to deplete both pools and thus predicted identical distribution of SVs.

The effect of EGTA (5 mM) on presynaptic Ca^{2+} currents in the functionally mature calyx

Although 5 mM EGTA had a minimal effect on P16–P19 release kinetics, 5 mM EGTA, but not 20 mM EGTA, resulted in a slight increase in presynaptic I_{Ca} amplitudes. Because slight changes in intracellular $[Ca^{2+}]$ can have large impacts on release rates, we examined whether the increased internal $[EGTA]_i$ alters VGCC properties and mask the EGTA effect on the RRP release rates. Although it is known at the P9–P11 calyx that Ca^{2+} buffer concentrations within the terminal impact Ca^{2+}-dependent inactivation and facilitation (Lin et al., 2012), this remained unknown at P16–P19 calyces. Therefore, we characterized the EGTA effect on I_{Ca} at the P9–P11 calyx. Analysis of current to voltage (I/V) relationship of the I_{Ca} revealed the following: (1) the amplitude of steady-state I_{Ca} became smaller from −50 mV to −20 mV; and (2) a slight rightward shift occurred in the activation kinetics in the presence of 5 mM EGTA at P9–P11 (Fig. 8A,C1,C2). In contrast, at P16–P19, the activation of I_{Ca} occurred at more negative voltages in the presence of 5 mM EGTA, although current amplitudes for voltage steps >0 mV were similar (Fig. 8B,D1,D2). Additionally, we also measured the peak amplitude of the Ca^{2+} tail currents. We found that 5 mM EGTA resulted in similar tail
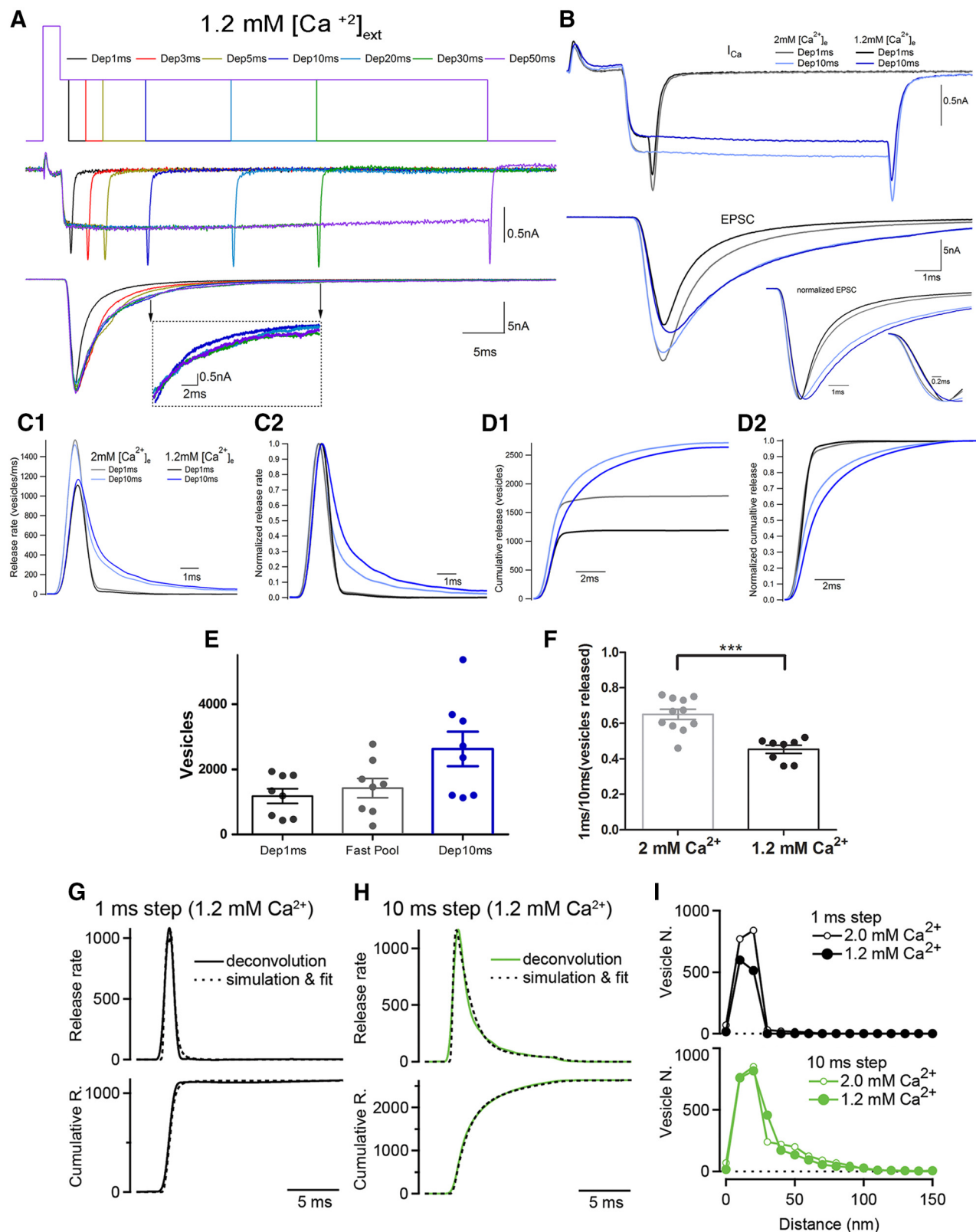
Figure 7. The 1.2 mM [Ca^{2+}]$_{ext}$ slower synaptic transmission and synaptic vesicles release kinetics at the P16–P19 calyx of Held. **A**, Stimulation protocol (top) and resulting presynaptic I$_{Ca}$ (middle) and EPSCs (bottom). Dashed line box represents a magnified view of the decaying EPSCs. Two arrows indicate the time window of the magnified EPSCs. **B**, Average traces of I$_{Ca}$ (top) and corresponding average traces of EPSCs (bottom) from 2 mM and 1.2 mM Ca^{2+} group. Inset, Normalized EPSCs and the rising phase of the EPSCs. **C**, Average release rate (**C1**) and normalized peak release rate (**C2**). **D**, Average cumulative release (**D1**) and normalized cumulative release (**D2**). **E**, Summary for SVs released by Dep1 ms and Dep10 ms in 1.2 mM Ca^{2+}. The numbers of fast-releasing SVs released by Dep10 ms are shown as fast pool. **F**, Comparison of the ratio of number of SVs released by Dep1 ms to Dep10 ms in 2 mM and 1.2 mM Ca^{2+}. ***$p < 0.001$. **E**, **F**, Data are presented as mean ± SEM. **G**, Deconvolution traces in P16–P19 calyces for 1 ms step in the presence of 1.2 mM Ca^{2+} were fit with simulated single vesicle release and cumulative release rates. **H**, Same as **G**, but for 10 ms step. **I**, Spatial distributions of SVs released in 1.2 mM Ca^{2+}. Traces from 2 mM Ca^{2+} shown for comparison were identical to those in Figure 3C.
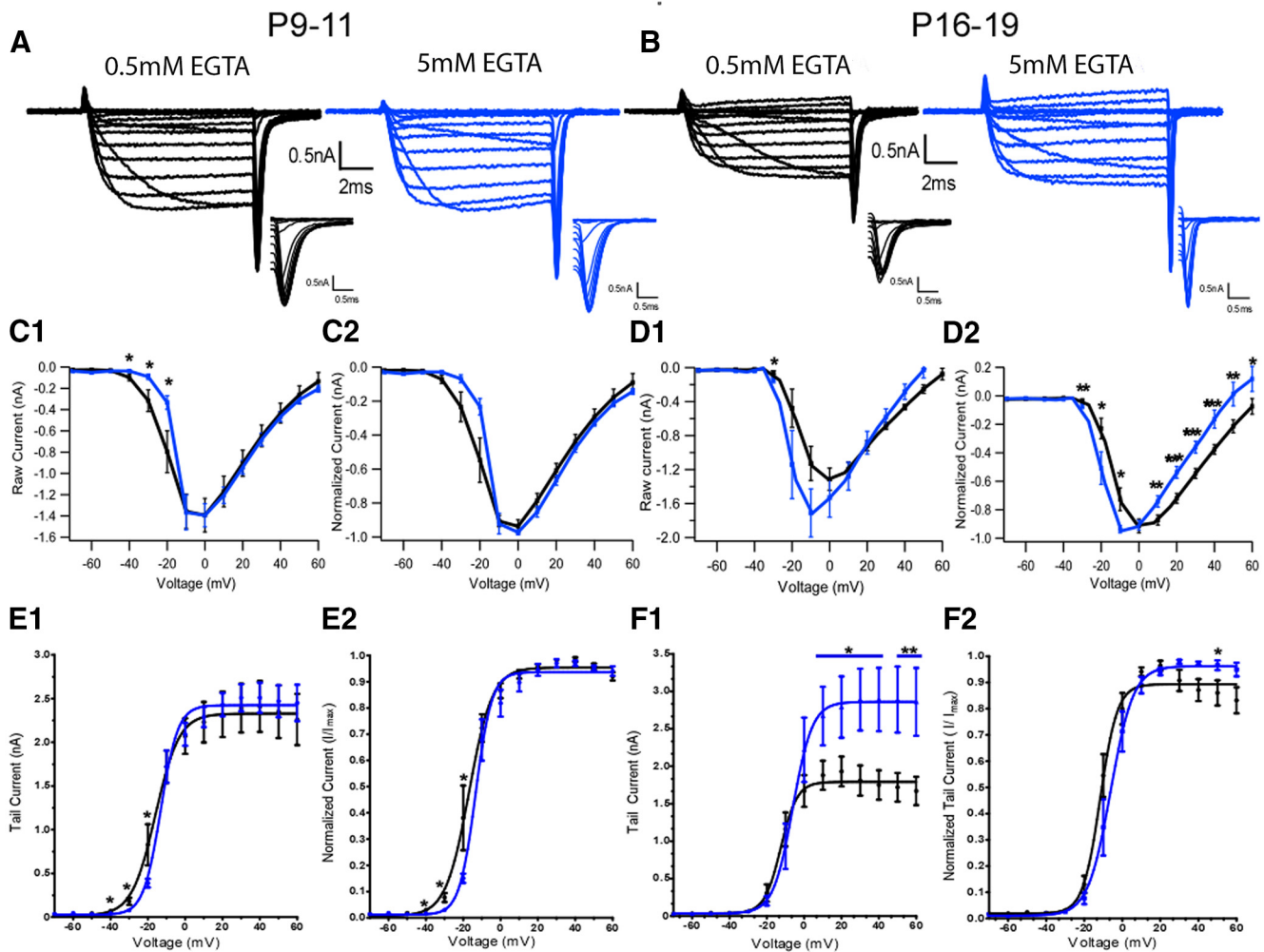
Figure 8. Effect of increasing [EGTA]$_i$ concentration to 5 mM on the I$_{Ca}$ kinetics at the P16−P19 calyx of Held. **A**, **B**, Representative I$_{Ca}$ traces for current/voltage (I/V) curve analysis from −70 mV to 60 mV at 0.5 mM EGTA and 5 mM EGTA, respectively, from immature and mature calyx of Held. Insets, Tail currents at the abovementioned voltages. **C1**, I/V plot representing the average I$_{Ca}$ amplitudes at steady state plotted against voltage. **C2**, Normalized average raw I$_{Ca}$ amplitudes at steady state (I/I$_{max}$) against voltage in immature calyces. **D1**, **D2**, Identical plots in mature synapses. **E**, **F**, Represent analysis of voltage-dependent activation of VGCCs. Activation curves were obtained from tail currents evoked by a 10 ms step to various membrane potentials from −70 mV to 60 mV. Data obtained with 0.5 mM EGTA (n = 7) and 5 mM (n = 8) in P9−P11 and 0.5 mM EGTA (n = 14) and 5 mM (n = 11) in P16−P19 were plotted against voltage and fitted by the Boltzmann function I = 1/(I$_{max}$ + exp (V$^{1/2}$ − V)/k), where V$^{1/2}$ and k represent the half-activation voltage and slope factor, respectively, in **E1** and **F1** for P9−P11 and P16−P19 calyces, respectively. The tail currents were normalized to the maximal value (I/I$_{max}$) for **E2** and **F2**, before Boltzmann fit. The currents were statistically compared by unpaired Student's t test. Data are presented as mean ± SEM.

currents amplitude at all voltages tested for P9–P11 (Fig. 8E1). However, in P16–P19 calyces, the tail currents amplitudes were >0 mV (Fig. 8F1). I/V relationship of the tail current and its fit with a Boltzmann function revealed a rightward shift in the half-activation voltage in P9–P11 calyces from −12.0 ± 0.8 mV (n = 15, 0.5 mM EGTA) to −5.8 ± 0.3 mV (n = 12, 5 mM EGTA) and a slightly faster kinetics of activation in P16–P19 calyces (5.6 ± 0.2; n = 12; 5 mM EGTA) versus (4.3 ± 0.7; n = 15; 0.5 mM EGTA) (Fig. 8E2,F2).

Although the increased [EGTA]$_i$ facilitated Ca^{2+} tail currents at positive voltages, these were in response to a 10 ms step. Previous studies at immature calyces have demonstrated that prede-polarization steps can increase I$_{Ca}$ (Awatramani et al., 2005; Hori and Takahashi, 2009); therefore, it remained unknown whether Ca^{2+} influx triggered by AP would be affected by increased [EGTA]$_i$. To test this, we recorded I$_{Ca}$ evoked by pseudo-AP waveforms in both [EGTA]$_i$ (Yang and Wang, 2006). Figure 9 reveals that the increase in [EGTA]$_i$ did not affect I$_{Ca}$ amplitude and charge evoked by AP-like waveforms P16–P19 calyx terminals. Finally, there was no change in peak steady state I$_{Ca}$

at 0 mV, indicating that our RRP measurements in the presence of 5 mM [EGTA]$_i$ are not caused by the increases in I$_{Ca}$.

Discussion

Using whole-cell paired recordings in combination with decon-volution analysis and an established VGCC to Ca^{2+} sensor model, we elucidated the alterations in the RRP that contribute to accelerated SV release kinetics and that underpin the early stages of auditory processing at the functionally mature calyx of Held terminal (P16–P19). Our results are in agreement with previous studies demonstrating developmental increase in SV release efficacy in response to APs (Taschenberger and von Gersdorff, 2000; Taschenberger et al., 2002; Renden and von Gersdorff, 2007; Wang et al., 2008; Kochubey et al., 2009). In the P9–P11 calyx, a 3 ms and a 30 ms step depletes the fast pool and total RRP, respectively (Lee et al., 2012). In contrast, we demonstrate, at the P16–P19 calyx, that a 1 ms step was sufficient to release the fast pool, whereas a 10 ms step was necessary to deplete the entire RRP (Figs. 1 and 2). Using our RRP size estimates from the 10 ms step (Figs. 1, 4, and 7) and dividing by reported AZ numbers
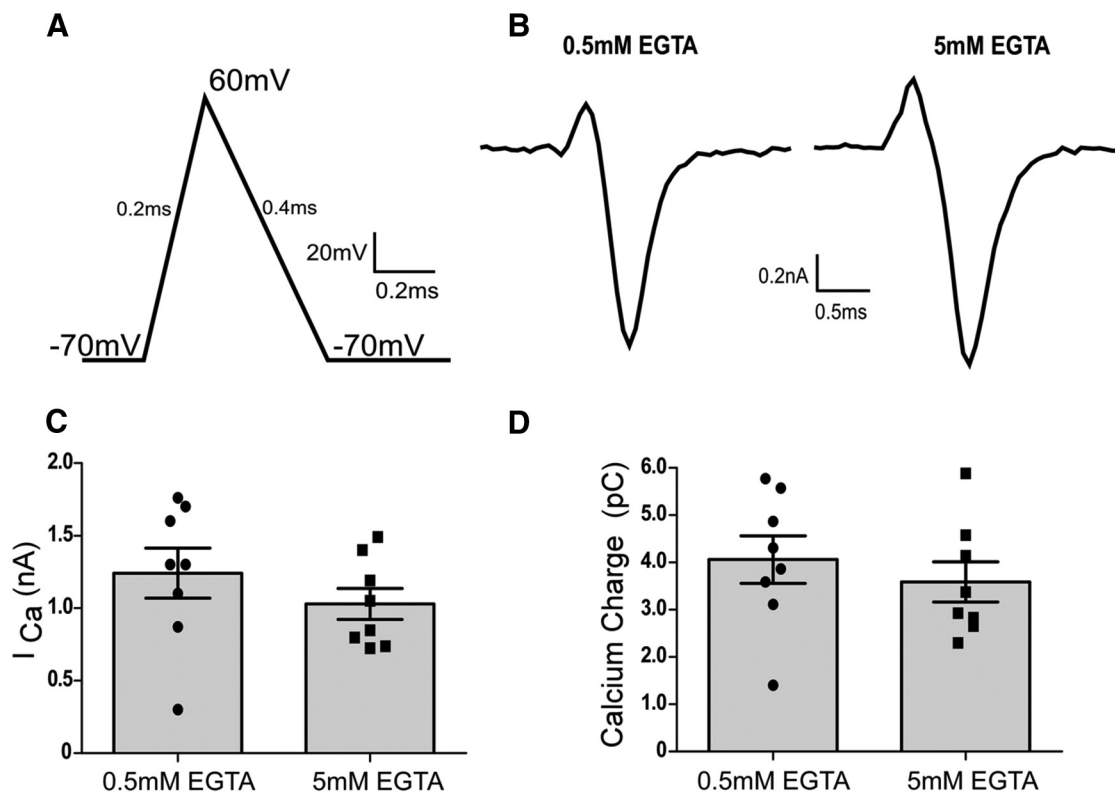
Figure 9. Effect of AP-like depolarization on the properties of I_{Ca} in the P16–P19 calyx of Held with 0.5 and 5 mM EGTA. ***A***, The stimulus protocol used for the experiment. The depolarization time was 0.2 ms with the repolarization phase at 0.4 ms. ***B***, Representative Ca^{2+} current waves obtained at 0.5 and 5 mM EGTA concentration in mature calyx of Held. ***C***, I_{Ca} were compared at the two concentrations of $[EGTA]_i$ when depolarized at 0.2 ms duration and plotted as a scatter plot ($n = 8$ each). ***D***, I_{Ca} charge at 0.5 and 5 mM EGTA concentrations ($n = 8$ each). Data is presented as mean $\pm$ SEM.

(Taschenberger et al., 2002), we estimate there are ~2–6 releasable SVs per AZ, consistent with earlier estimates of docked SVs per AZ from P9, P14, and P16 rats (Sätzler et al., 2002; Taschenberger et al., 2002; Horstmann et al., 2012).

A cellular mechanism of RRP release kinetics
Using numerical simulations of buffered Ca^{2+} diffusion and a single synchronous SV release sensor (Nakamura et al., 2015), we demonstrate a broad distribution in the distance between the edge of VGCC clusters, and SVs can replicate the time course of experimentally derived RRP release rates corresponding to both fast and slow pools at P9–P11 or P16–P19 calyces (Fig. 3). The average VGCC-SV distance at the P16–P19 calyces was ~15 nm for fast pool SVs (evoked by the 1 ms pulse) and is similar to previous estimates of ~20 nm for AP-evoked release (Wang et al., 2009; Nakamura et al., 2015). Therefore, it is likely that SVs evoked by 1 ms step constitute the same pool as those involved in AP-evoked release. In line with this idea, the fast pool undergoes a developmental shortening of the average VGCC-SV distance similar to AP-evoked release (Wang et al., 2009; Nakamura et al., 2015). The VGCC-SV distance for the slow pool was estimated to be between 25 and 150 nm, and like SVs in the fast pool, undergoes a similar developmental tightening. In P16–P19 animals, the release rates measured with 20 mM EGTA in the presynaptic pipette were consistent with a preferential block of distal SVs. Because a typical AZ diameter is ~300 nm (calculated from Taschenberger et al., 2002) and EM evidence suggests on average 1 cluster per AZ comprising only 12% of the AZ area (Nakamura et al., 2015), our data are consistent with conclusion that both the close and distally coupled SVs are all located within the AZ (Taschenberger and von Gersdorff, 2000; Taschenberger et al., 2002).

Although molecular mechanisms for tightening of the AP-evoked release RRP are emerging (Hosoi et al., 2009; Young and Neher, 2009; Yang et al., 2010; Chen et al., 2013), the mechanisms underlying slow pool release remains unclear. Our simulations and analysis are consistent with a single fast sensor (Schneggenburger and Neher, 2000; Wang et al., 2008) at 25–150 nm away from VGCC clusters (Fig. 6). Differential Ca^{2+} sensitivity has been proposed as an alternative mechanisms for slow pool release (Wolfel et al., 2007). We cannot rule out that heterogeneous intrinsic Ca^{2+} sensitivity contributes to slow pool release. However, the contribution of a second Ca^{2+} sensor or sensors appears to affect delayed release events that occur well after depolarization steps (Sun et al., 2007; Babai et al., 2014). Alternatively, differences in the fast Ca^{2+} sensor copy number could also impact slow release rates (Dittrich et al., 2013). Nevertheless, our conclusions are well supported by data from the P8–P10 calyx, which demonstrated that only a twofold difference in intrinsic Ca^{2+} sensitivity between the fast and slow pool SVs cannot fully account for the 10-fold difference in release kinetics (Wadel et al., 2007).

Varying the $[Ca^{2+}]_{ext}$ at immature calyces influences the fraction of the SVs released by APs from the RRP, likely due to alterations in $[Ca^{2+}]$ domains around single channels (Weber et al., 2010; but see Meinrenken et al., 2002). Indeed, a 10 ms step fully released the fast pool and overcame the slightly slower release kinetics (Fig. 7), resulting in a similar total RRP. Our simulations show that longer depolarizations allow for $[Ca^{2+}]$ domains around clusters to extend longer distances thus allowing access to distal SVs (Fig. 2). Consistent with this finding, the estimated distances of the two SV pools were nearly identical in 2 mM or 1.2 mM Ca^{2+} (Fig. 7). Such spatiotemporal dependence of $[Ca^{2+}]$
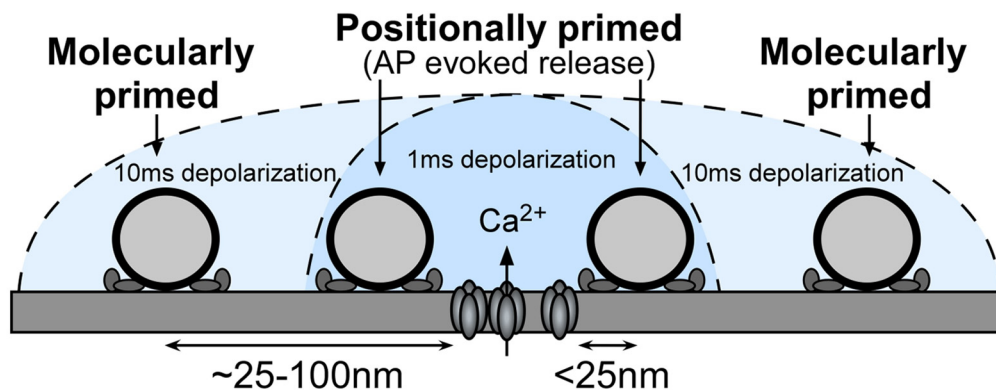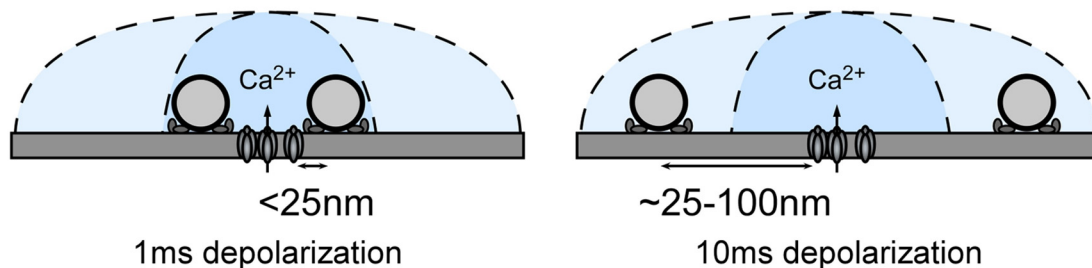
Figure 10. SV distribution within the P16–P19 calyx RRP. ***A***, ***B***, Schematic diagram showing SVs at different priming states located at different distance to the Ca²⁺ source. Only the SVs that locate close to the Ca²⁺ source can be released by AP. We propose that either a single AZ contains a mixture of fast and slow SVs (***A***) or that there are individual AZs within the calyx that contain only fast or only slow pool SVs (***B***). In both cases, we propose that distal SVs are rapidly converted to fast pool SVs for AP-evoked release to maintain signaling at high firing rates.

domains on the duration of the Ca²⁺ entry may account for why in P11–P14 calyces there is an apparent change in the RRP when using APs (Thanawala and Regehr, 2013).

Furthermore, because of the requirement of binding of multiple calcium ions to trigger SV fusion and high dependence on the $[Ca^{2+}]_{ext}$ (Schneggenburger and Neher, 2000; Bischofberger et al., 2002), lowering the $[Ca^{2+}]_{ext}$ would result in a slowdown in the onset of fusion. Supporting this hypothesis, we observed a 100 μs increase in the synaptic delay in 1.2 mM Ca²⁺ compared with 2 mM Ca²⁺ group, which is also predicted by simulations (120 μs increase in synaptic delay at 20 nm distance from VGCC cluster perimeter). This delay is assumed to be due to Ca²⁺ ion binding and subsequent initiation of fusion. However, recent reports of postpriming maturation of SVs, which lowers the activation energy required for SV fusion may also be Ca²⁺ dependent (Basu et al., 2007; Lee et al., 2013). Thus this increase in the synaptic delay may correlate to a possible Ca²⁺ dependency of postpriming.

In other model systems, evidence exists for a single VGCC opening triggering SV release (Stanley, 1993), and it has been hypothesized that VGCC numbers can modulate AP-evoked release (Bertram et al., 1996; Gentile and Stanley, 2005). At the calyx, the number of channels per cluster is highly variable (2–73) and on average ~20 (Nakamura et al., 2015). Thus, a small fraction of clusters (<20%) would exhibit one channel opening per AP (open probability 0.2) (Sheng et al., 2012). When a single VGCC opens, our model suggests that SVs located in the fast pool (20 nm) would have a low release probability (<0.03) (Nakamura et al., 2015). Although possible, single-channel release events are not the dominant mode of AP-evoked release at the calyx of Held as the P16–P19 calyx uses multiple VGCCs to trigger release of SVs in response to an AP (Fedchyshyn and Wang, 2005). To understand SV release in response to step depolarizations, we simulated 24 channels, a value close to the mean number of VGCCs per cluster (Nakamura et al., 2015), and showed that the fast pool is comprised of SVs tightly coupled to the cluster perimeter (Fig. 2). For 10 ms step depolarizations, the [Ca²⁺] at a distance is increased sufficiently to trigger release at distances up to 100 nm in P16–P19 animals (Fig. 2). Thus, open VGCCs clusters likely mediate release from both pools. Nevertheless, for the rarely observed isolated single channels (<3% of all detected channels) (Nakamura et al., 2015), longer depolarizations could mediate SV release (simulations not shown).

Implications for the calyx's ability to drive MNTB spiking over a wide range of firing rates

To support the encoding of auditory information, the posthearing calyx drives the spiking in the MNTB neuron over a broad range of firing rates, with little to no contribution from asynchronous release (Taschenberger et al., 2005; Scheuss et al., 2007). Because the AP waveform is very narrow, even during high firing rates at the posthearing calyx (Taschenberger and von Gersdorff,

2000), it is likely that only SVs tightly coupled to VGCCs (<25 nm) will be released in response to auditory stimulation. Although our data cannot discriminate whether fast and slow SVs exist at a single release site (Fig. 10*A*) or whether there are individual release sites that consist solely of either fast or slow SVs (Fig. 10 *B*), the slow SVs likely have physiological significance. Recent work has shown slow pool SVs can be rapidly converted (<80 ms) into fast pool SVs (Lee et al., 2012), through positional priming that drives these distal SVs close to VGCCs (Neher and Sakaba, 2008). Despite endocytosis rates at P14-P18 calyces being faster than prehearing calyces, they are on the orders of seconds (Kushmerick et al., 2006; Renden and von Gersdorff, 2007) and are too slow to follow rapid firing rate fluctuations (timescale of milliseconds) experienced by the calyx. Thus, we hypothesize that the slow pool contributes to a rapid SV replenishment for AP-evoked release to maintain spiking of MNTB in response to rapid firing rate changes in response to acoustic stimulation. Although the molecular mechanism that accounts for the rapid conversion from slow to fast pool SVs is poorly defined, Munc13s (Chen et al., 2013; Lipstein et al., 2013) and actin network (Lee et al., 2012) might play a role.

Slow pool conversion a general mechanism for sustaining signaling at high AP firing rates

Relative positioning of VGCC to SVs coupling and control of SV release kinetics for AP-evoked release was first proposed more than a quarter century ago (Yoshikami et al., 1989; Augustine, 1990; Adler et al., 1991; Stanley, 1993) and has been well studied in the calyx of Held (Sakaba and Neher, 2001b; Meinrenken et al., 2002; Fedchyshyn and Wang, 2005; Sakaba et al., 2005; Sakaba, 2006; Wadel et al., 2007; Neher and Sakaba, 2008; Wang et al., 2008; Young and Neher, 2009; Neher, 2010; Lee et al., 2012). Despite being considered as a specialized synapse, the calyx of Held release properties are very similar to a wide variety of model systems (Borst, 2010; Eggermann et al., 2011). Indeed, a number of synapses within the CNS and PNS from invertebrates to vertebrates have biphasic recovery rates of replenishment of SVs within the RRP with recovery time constants of tens of milliseconds and seconds that are matched with the recovery rate at the calyx (Hallermann and Silver, 2013), suggesting that a slow pool may also exist in other synapses. Interestingly, these fast recovery time constants are at minimum ~50-fold faster than SV recovery rates through endocytosis (Wu et al., 2014). Because positional priming is the rate-limiting step for SV availability for AP-evoked release, it is possible that fast recovery time constants represent the SV positioning rate at the close proximity of the edge of VGCC clusters. Therefore, the regulation of positional priming may be necessary to alter the reliability of a synapse to meet the functional demands of the circuit within which it is embedded.

References

Adler EM, Augustine GJ, Duffy SN, Charlton MP (1991) Alien intracellular calcium chelators attenuate neurotransmitter release at the squid giant synapse. J Neurosci 11:1496–1507. Medline

Allbritton NL, Meyer T, Stryer L (1992) Range of messenger action of calcium ion and inositol 1,4,5-trisphosphate. Science 258:1812–1815. CrossRef Medline

Armstrong CM, Bezanilla F (1974) Charge movement associated with the opening and closing of the activation gates of the Na channels. J Gen Physiol 63:533–552. CrossRef Medline

Augustine GJ (1990) Regulation of transmitter release at the squid giant synapse by presynaptic delayed rectifier potassium current. J Physiol 431: 343–364. CrossRef Medline

Awatramani GB, Price GD, Trussell LO (2005) Modulation of transmitter release by presynaptic resting potential and background calcium levels. Neuron 48:109–121. CrossRef Medline

Babai N, Kochubey O, Keller D, Schneggenburger R (2014) An alien divalent ion reveals a major role for Ca^{2+} buffering in controlling slow transmitter release. J Neurosci 34:12622–12635. CrossRef Medline

Basu J, Betz A, Brose N, Rosenmund C (2007) Munc13–1 C1 domain activation lowers the energy barrier for synaptic vesicle fusion. J Neurosci 27:1200–1210. CrossRef Medline

Baylor SM, Hollingworth S (1998) Model of sarcomeric Ca^{2+} movements, including ATP Ca^{2+} binding and diffusion, during activation of frog skeletal muscle. J Gen Physiol 112:297–316. CrossRef Medline

Bertram R, Sherman A, Stanley EF (1996) Single-domain/bound calcium hypothesis of transmitter release and facilitation. J Neurophysiol 75: 1919–1931. Medline

Bischofberger J, Geiger JR, Jonas P (2002) Timing and efficacy of Ca^{2+} channel activation in hippocampal mossy fiber boutons. J Neurosci 22: 10593–10602. Medline

Bollmann JH, Sakmann B, Borst JG (2000) Calcium sensitivity of glutamate release in a calyx-type terminal. Science 289:953–957. CrossRef Medline

Borst JG (2010) The low synaptic release probability in vivo. Trends Neurosci 33:259–266. CrossRef Medline

Borst JG, Soria van Hoeve J (2012) The calyx of Held synapse: from model synapse to auditory relay. Annu Rev Physiol 74:199–224. CrossRef Medline

Chen Z, Cooper B, Kalla S, Varoqueaux F, Young SM Jr (2013) The Munc13 proteins differentially regulate readily releasable pool dynamics and calcium-dependent recovery at a central synapse. J Neurosci 33:8336–8351. CrossRef Medline

DiGregorio DA, Peskoff A, Vergara JL (1999) Measurement of action potential-induced presynaptic calcium domains at a cultured neuromuscular junction. J Neurosci 19:7846–7859. Medline

DiGregorio DA, Rothman JS, Nielsen TA, Silver RA (2007) Desensitization properties of AMPA receptors at the cerebellar mossy fiber granule cell synapse. J Neurosci 27:8344–8357. CrossRef Medline

Dittrich M, Pattillo JM, King JD, Cho S, Stiles JR, Meriney SD (2013) An excess-calcium-binding-site model predicts neurotransmitter release at the neuromuscular junction. Biophys J 104:2751–2763. CrossRef Medline

Eggermann E, Bucurenciu I, Goswami SP, Jonas P (2011) Nanodomain coupling between Ca^{2+} channels and sensors of exocytosis at fast mammalian synapses. Nat Rev Neurosci 13:7–21. CrossRef Medline

Fedchyshyn MJ, Wang LY (2005) Developmental transformation of the release modality at the calyx of Held synapse. J Neurosci 25:4131–4140. CrossRef Medline

Gentile L, Stanley EF (2005) A unified model of presynaptic release site gating by calcium channel domains. Eur J Neurosci 21:278–282. CrossRef Medline

Grothe B, Pecka M, McAlpine D (2010) Mechanisms of sound localization in mammals. Physiol Rev 90:983–1012. CrossRef Medline

Hallermann S, Silver RA (2013) Sustaining rapid vesicular release at active zones: potential roles for vesicle tethering. Trends Neurosci 36:185–194. CrossRef Medline

Haydon PG, Henderson E, Stanley EF (1994) Localization of individual calcium channels at the release face of a presynaptic nerve terminal. Neuron 13:1275–1280. CrossRef Medline

Helmchen F, Borst JG, Sakmann B (1997) Calcium dynamics associated with a single action potential in a CNS presynaptic terminal. Biophys J 72:1458–1471. CrossRef Medline

Hori T, Takahashi T (2009) Mechanisms underlying short-term modulation of transmitter release by presynaptic depolarization. J Physiol 587: 2987–3000. CrossRef Medline

Horstmann H, Korber C, Sätzler K, Aydin D, Kuner T (2012) Serial section scanning electron microscopy (S3EM) on silicon wafers for ultra-structural volume imaging of cells and tissues. PLoS One 7:e35172. CrossRef Medline

Hosoi N, Holt M, Sakaba T (2009) Calcium dependence of exo- and endocytotic coupling at a glutamatergic synapse. Neuron 63:216–229. CrossRef Medline

Joshi I, Shokralla S, Titis P, Wang LY (2004) The role of AMPA receptor gating in the development of high-fidelity neurotransmission at the calyx of Held synapse. J Neurosci 24:183–196. CrossRef Medline

Klingauf J, Neher E (1997) Modeling buffered Ca^{2+} diffusion near the membrane: implications for secretion in neuroendocrine cells. Biophys J 72:674–690. CrossRef Medline

Kochubey O, Han Y, Schneggenburger R (2009) Developmental regulation of the intracellular Ca^{2+} sensitivity of vesicle fusion and Ca^{2+}-secretion coupling at the rat calyx of Held. J Physiol 587:3009–3023. CrossRef Medline

Kushmerick C, Renden R, von Gersdorff H (2006) Physiological temperatures reduce the rate of vesicle pool depletion and short-term depression

via an acceleration of vesicle recruitment. J Neurosci 26:1366–1377. CrossRef Medline

Lee JS, Ho WK, Lee SH (2012) Actin-dependent rapid recruitment of reluctant synaptic vesicles into a fast-releasing vesicle pool. Proc Natl Acad Sci U S A 109:E765–E774. CrossRef Medline

Lee JS, Ho WK, Neher E, Lee SH (2013) Superpriming of synaptic vesicles after their recruitment to the readily releasable pool. Proc Natl Acad Sci U S A 110:15079–15084. CrossRef Medline

Lin KH, Erazo-Fischer E, Taschenberger H (2012) Similar intracellular Ca^{2+} requirements for inactivation and facilitation of voltage-gated Ca^{2+} channels in a glutamatergic mammalian nerve terminal. J Neurosci 32:1261–1272. CrossRef Medline

Lipstein N, Sakaba T, Cooper BH, Lin KH, Strenzke N, Ashery U, Rhee JS, Taschenberger H, Neher E, Brose N (2013) Dynamic control of synaptic vesicle replenishment and short-term plasticity by Ca(2+)-calmodulin-Munc13–1 signaling. Neuron 79:82–96. CrossRef Medline

Lorteije JA, Rusu SI, Kushmerick C, Borst JG (2009) Reliability and precision of the mouse calyx of Held synapse. J Neurosci 29:13770–13784. CrossRef Medline

Lou X, Scheuss V, Schneggenburger R (2005) Allosteric modulation of the presynaptic Ca^{2+} sensor for vesicle fusion. Nature 435:497–501. CrossRef Medline

Meinrenken CJ, Borst JGG, Sakmann B (2002) Calcium secretion coupling at calyx of Held governed by nonuniform channel-vesicle topography. J Neurosci 22:1648–1667. Medline

Nägerl UV, Novo D, Mody I, Vergara JL (2000) Binding kinetics of calbindin-D(28k) determined by flash photolysis of caged Ca(2+). Biophys J 79:3009–3018. CrossRef Medline

Nakamura Y, Harada H, Kamasawa N, Matsui K, Rothman JS, Shigemoto R, Silver RA, DiGregorio DA, Takahashi T (2015) Nanoscale distribution of presynaptic Ca^{2+} channels and its impact on vesicular release during development. Neuron 85:145–158. CrossRef Medline

Neher E (2010) What is rate-limiting during sustained synaptic activity: vesicle supply or the availability of release sites. Front Synaptic Neurosci 2:144. Medline

Neher E, Sakaba T (2001a) Estimating transmitter release rates from postsynaptic current fluctuations. J Neurosci 21:9638–9654. Medline

Neher E, Sakaba T (2001b) Combining deconvolution and noise analysis for the estimation of transmitter release rates at the calyx of Held. J Neurosci 21:444–461. Medline

Neher E, Sakaba T (2008) Multiple roles of calcium ions in the regulation of neurotransmitter release. Neuron 59:861–872. CrossRef Medline

Nielsen TA, DiGregorio DA, Silver RA (2004) Modulation of glutamate mobility reveals the mechanism underlying slow-rising AMPAR EPSCs and the diffusion coefficient in the synaptic cleft. Neuron 42:757–771. CrossRef Medline

Renden R, von Gersdorff H (2007) Synaptic vesicle endocytosis at a CNS nerve terminal: faster kinetics at physiological temperatures and increased endocytotic capacity during maturation. J Neurophysiol 98:3349–3359. CrossRef Medline

Renden R, Taschenberger H, Puente N, Rusakov DA, Duvoisin R, Wang LY, Lehre KP, von Gersdorff H (2005) Glutamate transporter studies reveal the pruning of metabotropic glutamate receptors and absence of AMPA receptor desensitization at mature calyx of Held synapses. J Neurosci 25:8482–8497. CrossRef Medline

Sakaba T (2006) Roles of the fast-releasing and the slowly releasing vesicles in synaptic transmission at the calyx of Held. J Neurosci 26:5863–5871. CrossRef Medline

Sakaba T, Neher E (2001a) Preferential potentiation of fast-releasing synaptic vesicles by cAMP at the calyx of Held. Proc Natl Acad Sci U S A 98:331–336. CrossRef Medline

Sakaba T, Neher E (2001b) Quantitative relationship between transmitter release and calcium current at the calyx of Held synapse. J Neurosci 21:462–476. Medline

Sakaba T, Neher E (2001c) Calmodulin mediates rapid recruitment of fast-releasing synaptic vesicles at a calyx-type synapse. Neuron 32:1119–1131. CrossRef Medline

Sakaba T, Stein A, Jahn R, Neher E (2005) Distinct kinetic changes in neurotransmitter release after SNARE protein cleavage. Science 309:491–494. CrossRef Medline

Sätzler K, Söhl LF, Bollmann JH, Borst JG, Frotscher M, Sakmann B, Lübke JH (2002) Three-dimensional reconstruction of a calyx of Held and its

postsynaptic principal neuron in the medial nucleus of the trapezoid body. J Neurosci 22:10567–10579. Medline

Scheuss V, Taschenberger H, Neher E (2007) Kinetics of both synchronous and asynchronous quantal release during trains of action potential-evoked EPSCs at the rat calyx of Held. J Physiol 585:361–381. CrossRef Medline

Schneggenburger R, Neher E (2000) Intracellular calcium dependence of transmitter release rates at a fast central synapse. Nature 406:889–893. CrossRef Medline

Schneggenburger R, Han Y, Kochubey O (2012) Ca(2+) channels and transmitter release at the active zone. Cell Calcium 52:199–207. CrossRef Medline

Sheng J, He L, Zheng H, Xue L, Luo F, Shin W, Sun T, Kuner T, Yue DT, Wu LG (2012) Calcium-channel number critically influences synaptic strength and plasticity at the active zone. Nat Neurosci 15:998–1006. CrossRef Medline

Sonntag M, Englitz B, Kopp-Scheinpflug C, Rübsamen R (2009) Early postnatal development of spontaneous and acoustically evoked discharge activity of principal cells of the medial nucleus of the trapezoid body: an in vivo study in mice. J Neurosci 29:9510–9520. CrossRef Medline

Sonntag M, Englitz B, Typlt M, Rübsamen R (2011) The calyx of Held develops adult-like dynamics and reliability by hearing onset in the mouse in vivo. J Neurosci 31:6699–6709. CrossRef Medline

Stanley EF (1993) Single calcium channels and acetylcholine release at a presynaptic nerve terminal. Neuron 11:1007–1011. CrossRef Medline

Sun J, Pang ZP, Qin D, Fahim AT, Adachi R, Südhof TC (2007) A dual-Ca^{2+}-sensor model for neurotransmitter release in a central synapse. Nature 450:676–682. CrossRef Medline

Taschenberger H, von Gersdorff H (2000) Fine-tuning an auditory synapse for speed and fidelity: developmental changes in presynaptic waveform, EPSC kinetics, and synaptic plasticity. J Neurosci 20:9162–9173. Medline

Taschenberger H, Leão RM, Rowland KC, Spirou GA, von Gersdorff H (2002) Optimizing synaptic architecture and efficiency for high-frequency transmission. Neuron 36:1127–1143. CrossRef Medline

Taschenberger H, Scheuss V, Neher E (2005) Release kinetics, quantal parameters and their modulation during short-term depression at a developing synapse in the rat CNS. J Physiol 568:513–537. CrossRef Medline

Thanawala MS, Regehr WG (2013) Presynaptic calcium influx controls neurotransmitter release in part by regulating the effective size of the readily releasable pool. J Neurosci 33:4625–4633. CrossRef Medline

Wadel K, Neher E, Sakaba T (2007) The coupling between synaptic vesicles and Ca^{2+} channels determines fast neurotransmitter release. Neuron 53:563–575. CrossRef Medline

Wang LY, Neher E, Taschenberger H (2008) Synaptic vesicles in mature calyx of Held synapses sense higher nanodomain calcium concentrations during action potential-evoked glutamate release. J Neurosci 28:14450–14458. CrossRef Medline

Wang LY, Fedchyshyn MJ, Yang YM (2009) Action potential evoked transmitter release in central synapses: insights from the developing calyx of Held. Mol Brain 2:36. CrossRef Medline

Weber AM, Wong FK, Tufford AR, Schlichter LC, Matveev V, Stanley EF (2010) N-type Ca^{2+} channels carry the largest current: implications for nanodomains and transmitter release. Nat Neurosci 13:1348–1350. CrossRef Medline

Wölfel M, Lou X, Schneggenburger R (2007) A mechanism intrinsic to the vesicle fusion machinery determines fast and slow transmitter release at a large CNS synapse. J Neurosci 27:3198–3210. CrossRef Medline

Wu LG, Hamid E, Shin W, Chiang HC (2014) Exocytosis and endocytosis: modes, functions, and coupling mechanisms. Annu Rev Physiol 76:301–331. CrossRef Medline

Yang YM, Wang LY (2006) Amplitude and kinetics of action potential-evoked Ca^{2+} current and its efficacy in triggering transmitter release at the developing calyx of Held synapse. J Neurosci 26:5698–5708. CrossRef Medline

Yang YM, Fedchyshyn MJ, Grande G, Aitoubah J, Tsang CW, Xie H, Ackerley CA, Trimble WS, Wang LY (2010) Septins regulate developmental switching from microdomain to nanodomain coupling of Ca^{2+} influx to neurotransmitter release at a central synapse. Neuron 67:100–115. CrossRef Medline

Yoshikami D, Bagabaldo Z, Olivera BM (1989) The inhibitory effects of omega-conotoxins on Ca channels and synapses. Ann N Y Acad Sci 560:230–248. CrossRef Medline

Young SM Jr, Neher E (2009) Synaptotagmin has an essential function in synaptic vesicle positioning for synchronous release in addition to its role as a calcium sensor. Neuron 63:482–496. CrossRef Medline